Numerical and Experimental Investigation of the Neutral Atmospheric Surface Layer

PHILIPPE DROBINSKI,* PIERRE CARLOTTI,[+] JEAN-LUC REDELSPERGER,[#] ROBERT M. BANTA,[@]
VALERY MASSON,[#] AND ROB K. NEWSOM[@],[&]

*Institut Pierre Simon Laplace/Service d'Aéronomie, Paris, France
[+]Centre d'Études des Tunnels, Bron, France
[#]Centre National de Recherches Météorologiques, Météo-France, Toulouse, France
[@]NOAA/Environmental Technology Laboratory, Boulder, Colorado
[&]Cooperative Institute for Research in the Atmosphere, Fort Collins, Colorado

ABSTRACT

This study combines the experimental measurements with large-eddy simulation (LES) data of a neutral planetary boundary layer (PBL) documented by a 60-m tower instrumented with eight sonic anemometers, and a high-resolution Doppler lidar during the 1999 Cooperative Atmospheric and Surface Exchange Study (CASES-99) experiment. The target of the paper is (i) to investigate the multiscale nature of the turbulent eddies in the surface layer (SL), (ii) to explain the existence of a -1 power law in the velocity fluctuation spectra, and (iii) to investigate the different nature of turbulence in the two sublayers within the SL, which are the eddy surface layer (ESL; lower sublayer of the SL lying between the surface and about 20-m height) and the shear surface layer (SSL; lying between the ESL top and the SL top). The sonic anemometers and Doppler lidar prove to be proper instruments for LES validation, and in particular, the Doppler lidar because of its ability to map near-surface eddies.

This study shows the different nature of turbulence in the ESL and the SSL in terms of organized eddies, velocity fluctuation spectra, and second-order moment statistics. If quantitative agreement is found in the SSL between the LES and the measurements, only qualitative similarity is found in the ESL due to the subgrid-scale model, indicating that the LES captures part of the physics of the ESL. The LES helps explain the origin of the -1 power-law spectral subrange evidence in the velocity fluctuation spectra computed in the SL using the CASES-99 dataset: strong interaction between the mean flow and the fluctuating vorticities is found in the SL, and turbulent production is found to be larger than turbulent energy transfer for $k_1 z > 1$ (k_1 being the longitudinal wavenumber and z the height), which is the condition of the -1 power-law existence.

1. Introduction

Turbulence in the surface layer (SL), corresponding to the first hundred meters of the planetary boundary layer (PBL; even less in stable PBL), is one major process controlling energy (momentum, sensible, and latent heat), water vapor and pollutants exchanges between the surface and the PBL. The understanding of the nature of these exchanges, and their impact on the largest scales, are open fields of high priority research activity and their representation in numerical models is a major issue. In the present study, we focus on the neutral atmospheric SL because any atmospheric SL theory developed for nonneutral stratification must match in the limit the neutral case and because near-neutral conditions are frequently met above very rough surfaces such as forest and tall natural vegetation. LES is a common method to investigate PBL turbulent flows, and neutral PBL flows in particular (e.g., Deardorff 1972; Moeng and Sullivan 1994; Carlotti 2002; Drobinski and Foster 2003). However, in this type of PBL, the turbulent eddies are smaller than in the convective PBL case (for which its structure is dominated by large-scale thermals), and the inertial subrange is reached at higher wavenumbers. For given domain size and grid resolution, a larger impact of the subgrid-scale (SGS) formulation is thus expected in a neutral case than in the convective case (Nieuwstadt et al. 1992; Andren et al. 1994). This makes the neutral PBL more

difficult to simulate by the LES especially near the surface, where turbulence displays linear organization and anisotropic characteristics (e.g., Drobinski et al. 2004) and where until now, there was a lack of comparison with measurements. Despite the existing LES evaluations, Wyngaard and Peltier (1996) stress that systematic evaluation of LES results has been lacking, partly because of the difficulty to interpret the differences between LES and actual data and to assess model performance (Stevens and Lenschow 2001). In general, field experiments give access to time series of in situ measurements (e.g., with anemometers) or vertical cuts of the atmosphere (with radio soundings) whereas LES give three-dimensional fields, which are often interpreted in term of structures. A challenge is therefore to be able to compare these very different types of results. Developments in remote sensing technologies can provide opportunities for making more direct comparisons, as pointed out by Stevens and Lenschow (2001) and Drobinski and Foster (2003). Recently, remote sensing was used to investigate convective PBL and to test LES (Wulfmeyer 1999; Avissar et al. 1998; Mayor et al. 2003; Weinbrecht et al. 2004).

Notwithstanding the recent progress, the precise nature of neutral SL turbulence is still far from being understood. This includes the investigation of the vertical structure of the SL, the nature of the near-surface organized eddies and the associated energetics and momentum transport. This naturally requires a test of the ability of numerical model to reproduce the SL dynamics. To address these issues, the present papers combines the dataset of the 13 October 1999 collected during the CASES-99 field experiment and analyzed in Drobinski et al. (2004), with LES forced with similar meteorological conditions. The LES validation relies on the 60-m tower instrumented with eight sonic anemometers giving access to vertical profiles of mean and turbulent atmospheric variables and on the high-resolution Doppler lidar able to map in three dimensions the coherent structures in the PBL. The target of the present paper is therefore to (i) investigate the multiscale nature of the turbulent eddies in the SL; (ii) to explain the existence of a -1 power law in the velocity fluctuation spectra already shown in Drobinski et al. (2004); and (iii) to investigate the different nature of turbulence in the two sublayers within the SL defined by Drobinski et al. (2004), which are the eddy surface layer (ESL; lower sublayer of the SL lying between the surface and about 20 m height) and the shear surface layer (SSL; lying between the ESL top and the SL top).

In the present study, the model and measurements agree in many areas, including the dimensions of the larger eddies, many aspects of the velocity spectra, and ratios of quantities involving updrafts, downdrafts, and vertical momentum transport, thus giving confidence in the results from both approaches. Section 2 presents the selected CASES-99 case and the LES setup. In section 3, the multiscale eddy structure of the SL is discussed and the contribution of these eddies to momentum transport is addressed. To do so, comparison of the flow structure is performed by putting the LES data in a form similar to the Doppler lidar measurements, and comparison of conditional statistics of momentum fluxes is achieved. In section 4, the vertical profiles of spectra and variances are computed and compared to the CASES-99 data. The origin of the -1 power law in the measured and simulated velocity fluctuation spectra is proposed with the use of the validated LES data and discussed in relation with the neutral surface layer concept proposed by Drobinski et al. (2004). Section 5 concludes the study.

2. Presentation of the selected case

a. The CASES-99 experiment

The CASES-99 experiment was designed to be a nighttime experiment aimed at studying the stable boundary layer and physical processes associated with the morning and evening transition periods (Poulos et al. 2002). However, measurements were also taken in the afternoons, when neutral conditions are possible. The experimental period was from 1 to 31 October 1999 near Leon, Kansas, 50 km east of Wichita. The topography of the CASES-99 site is flat with shallow gullies and very gentle slopes covered with prairie grass about 0.5 m tall. These slopes can affect or generate flows at night, but are not a factor for the present study, where a neutral boundary layer characteristic of the afternoon was chosen.

The site was equipped with several meteorological towers, including one of 60-m. Eight sonic anemometers operated by the National Center for Atmospheric Research (NCAR) were mounted on the 60-m tower at heights of 1.5, 5, 10, 20, 30, 40, 50, and 55 m. The sonic anemometers operated more or less continuously during the entire month-long CASES-99 field program and provided three-component wind and temperature data at a sampling rate of 20 Hz. Radiosonde releases sampled atmospheric pressure, ambient temperature, and relative humidity at 1 Hz during ascent and transmitted these data to the ground with navigational aid signals from GPS. Wind measurements at the lowest levels, however, were subject to substantial error due to difficulties in establishing GPS lock. Data were also collected using the high-resolution Doppler lidar (HRDL) developed by the National Oceanic and At-

mospheric Administration—Environmental Technology Laboratory (NOAA/ETL) in cooperation with the NCAR—Atmospheric Technology Division (NCAR/ATD) and the Army Research Office (ARO).

HRDL is a scanning Doppler lidar system that provides range-resolved Doppler velocity and aerosol backscatter fields for near-surface and boundary layer studies (Grund et al. 2001), made possible by its good range resolution (30 m), velocity precision (0.1 m s^{-1}), and narrow beam. As described in Drobinski et al. (2004), HRDL was deployed during CASES-99 primarily to address the stable boundary layer objectives of that study (e.g., Banta et al. 2002, 2003; Poulos et al. 2002), but on several occasions it was operated during daylight or transition hours of the day, including the afternoon of 13 October analyzed in Drobinski et al. (2004). Scans performed during the two hours before sunset on that day included 360° azimuth scans at small elevation angles, which provide a very shallow cone of data centered on the lidar, and scans in elevation at a fixed direction, which provide a vertical slice of data. The nearly horizontal conical scans were used for surveying the horizontal structure and variability of the velocity field, and the vertical-slice scans, which were performed both parallel to and perpendicular to the mean wind direction, were used for analyzing the structure of the velocity field in a 2D vertical cross section of the PBL. Examples of a 1°-elevation conical scan and of a sequence of six cross-wind vertical-slice scans are presented in Drobinski et al. (2004, their Figs. 10 and 11).

b. The 13 October 1999 case

1) METEOROLOGICAL DESCRIPTION

The clear-sky, windy conditions on the afternoon of 13 October are described by Drobinski et al. (2004) based on tower data and the 1300 central standard time (CST; UTC − 6 h) sounding (Fig. 1). Boundary layer profiles of wind and potential temperature show a well mixed layer (ML) beneath a very strong 8-K capping inversion at 750 m AGL, which defines the PBL height h, and postfrontal northerly winds of about 10 m s^{-1}. In the first 150 m the wind varies between 5 m s^{-1} near the ground to 10 m s^{-1} so the near-surface vertical shear of the horizontal wind is about 3.3×10^{-2} s^{-1}. The SL is characterized by a logarithmic wind profile with no veering up to about 100 m, which we define as the top of the SL (Fig. 1). Strong postfrontal subsidence counteracted the growth by entrainment of the turbulent afternoon mixed layer, as a rawinsonde ascent at 1700 CST (2300 UTC) showed the inversion still at about 750 m (Fig. 1). After this time, however, both the heat flux and the near-surface wind speeds decreased signifi-
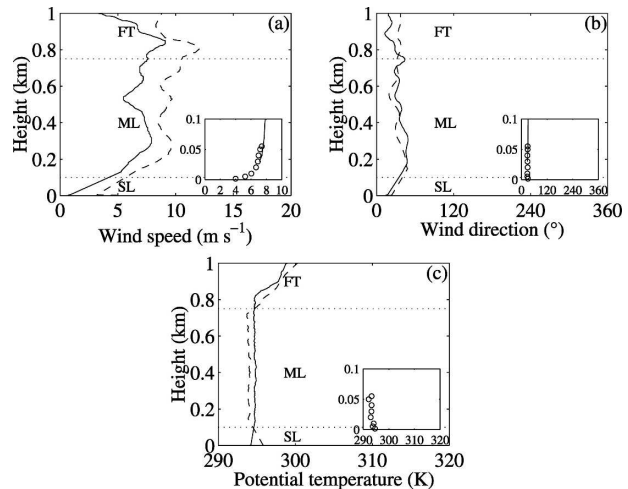

FIG. 1. Vertical profiles of (a) wind speed, (b) wind direction, and (c) potential temperature from the 1300 (solid line) and 1700 CST (dashed line) soundings on 13 Oct 1999. The subpanels are zooms of the vertical profiles of (a) mean wind speed, (b) direction, and (c) temperature in the 0.1-km-deep lower layer of the SL (caution, the wind speed scale is not the same in the main panel as in the zoomed subpanel). The solid line corresponds to the horizontally averaged mean wind speed and direction calculated from HRDL vertical-slice scans at about 1600 CST, whereas the circles correspond to the vertical profiles of wind speed and direction, and temperature recorded by the sonic anemometers up to 56 m height, and averaged over the 1600–1730 CST time period.

cantly, so that the subsidence caused the capping inversion to drop to 500 m AGL by 0200 CST (Fritts et al. 2003). Between 1600 and 1730 CST, which corresponds to the near-neutral time period studied by Drobinski et al. (2004), the surface momentum flux decreases from 0.28 m^2 s^{-2} down to 0.20 m^2 s^{-2} between 1600 and 1630 CST and then remains constant. The surface sensible heat flux drops from 60 W m^{-2} down to 0 between 1600 and 1630 CST, and then remains near 0. The night of 13/14 October was selected for intensive sampling, becoming intensive observing period (IOP)-6 of CASES-99. Prior to 1800 CST, mixed-layer winds continued to exceed 8 m s^{-1}, as both tower and balloon-sonde profile data showed the surface layer transitioning from weakly unstable to weakly stable, or in other words, during the two hours from 1600 to 1800 CST the lower boundary layer went from near-neutral with a slightly warmer surface to near-neutral with a slightly cooler surface.

2) SIMULATION SETUP

The LES was made using Méso–NH code (Lafore et al. 1998) with forcing similar to the 13 October 1999 case described above. The LES domain is 3 km long, 1 km wide, and 750 m high with 6.25-m grid resolution

(Carlotti 2002). The computing grid is cubic to avoid any influence of anisotropy of the grid with periodic boundary conditions on the lateral sides and a rigid lid at the top. The LES computes the spatially filtered version of the actual velocity field. The equation for the filtered velocity field [denoted by $\widetilde{(\cdot)}$] is given by

$$\begin{cases} \partial_t \tilde{u}_i + \partial_j \tilde{u}_i \tilde{u}_j = -\partial_i \tilde{p} - \partial_j \Gamma_{ij} + 2(\mathbf{\Omega} \times \tilde{\mathbf{u}})_i \\ \partial_i \tilde{u}_i = 0 \end{cases}, \quad (1)$$

where $\Gamma_{ij} = \widetilde{u_i u_j} - \tilde{u}_i \tilde{u}_j$, $u_1 = u$ is the longitudinal velocity fluctuation, $u_2 = v$ is the transverse velocity fluctuation, and $u_3 = w$ is the vertical velocity fluctuation. The term $2\mathbf{\Omega} \times \tilde{\mathbf{u}}$ represents the forcing of the flow by Coriolis forces and $\partial_j \Gamma_{ij}$ the SGS stresses. Méso–NH uses a 1.5-order closure with the subgrid kinetic energy $e = 0.5(\Gamma_{11} + \Gamma_{22} + \Gamma_{33})$ as a prognostic variable (Cuxart et al. 2000). By writing an empirical evolution equation on e and an equation relating e and Γ_{ij}, one gets:

$$\partial_t e = -\partial_k(\widetilde{u_k} e) - \Gamma_{ik} \partial_k \tilde{u}_i - \partial_j(C_{2m} L \sqrt{e} \partial_j e) - \varepsilon$$

$$\varepsilon = C_\varepsilon \frac{e^{3/2}}{L}$$

$$\Gamma_{ij} = \frac{2}{3} \delta_{ij} e - \frac{4}{15} \frac{L}{C_m} \sqrt{e} \left(\partial_j \tilde{u}_i + \partial_i \tilde{u}_j - \frac{2}{3} \delta_{ij} \partial_k \widetilde{u_k} \right), \quad (2)$$

where $C_m = 4$, $C_{2m} = 0.2$, and $C_\varepsilon = 0.7$ are nondimensional constants and $L = (\Delta x \Delta y \Delta z)^{1/3}$ is a length scale, where Δx, Δy, and Δz are the mesh sizes. In terms of a commonly used closure based on eddy viscosity $\nu = C_k L \sqrt{e}$, the coefficient C_k is linked to C_m by $C_k = 4/15 C_m^{-1}$. The values of C_k found in the literature vary but Krettenauer and Schumann (1992) found a weak sensitivity of LES results to the values of C_k in the commonly used range. The values $C_m = 4$ and $C_\varepsilon = 0.7$ are from Redelsperger and Sommeria (1981) and lead to $C_k = 0.067$. Schmidt and Schumann (1989) use $C_m = 3.5$ and $C_\varepsilon = 0.845$, which lead to $C_k = 0.076$ for our subgrid model. The calculation by Schmidt and Schumann (1989) leads to $C_\varepsilon/C_k = \pi^2$ so $C_k = 0.086$ when $C_\varepsilon = 0.845$. Deardorff (1980) used $C_k = 0.1$. The initial condition was a laminar geostrophic flow $U_g = 10 \text{ m s}^{-1}$ aligned along the x axis with small random temperature perturbations to generate turbulence. The horizontal velocities at the top of the domain are given by the geostrophic forcing. At the ground, the surface buoyancy flux is zero and the roughness length z_0 is imposed. The friction velocity u_* is computed from the assumption of a local log law, $u_* = k_0 \tilde{u}/\ln(x_3/z_0)$ at the height $x_3 = \Delta z/2$, where $\tilde{u} = \sqrt{\tilde{u}_1^2 + \tilde{u}_2^2}$ is the filtered streamwise velocity and $k_0 = 0.4$ is the von Kármán constant. The SGS kinetic energy e in the first cell close to the ground (at the height $\Delta z/2$) is calculated using Eq. (2a),
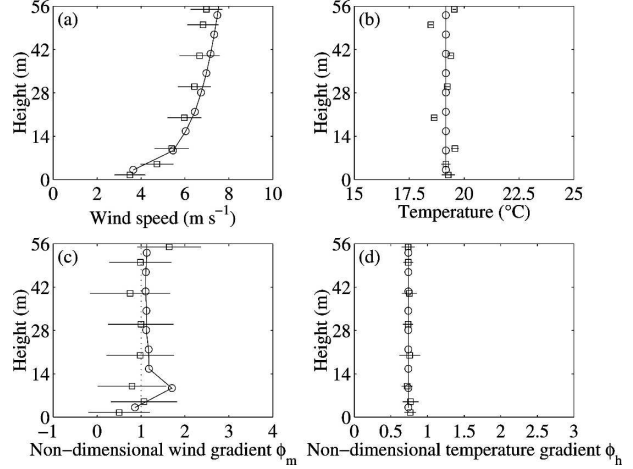

FIG. 2. Vertical profile of (a) wind speed, (b) temperature, (c) nondimensional wind gradient ϕ_m, and nondimensional temperature gradient ϕ_h computed from the sonic anemometer measurements averaged between 1600 and 1715 CST (box) compared to the Méso-NH profile (circle) using Eq. (3) ϕ_h and ϕ_m being equal to 0.74 and 1 in neutral conditions, respectively. The error bars indicate the $1 - \sigma$ statistical uncertainty.

where the term $\Gamma_{ik} \partial_k \tilde{u}_i$ is interpolated from its value at $x_3 = \Delta z + \Delta z/2$. This boundary condition is necessary because it is impossible to resolve the viscous sublayer, but it may introduce some spurious effects in the results, especially on the effective value of the roughness length when it is computed a posteriori from the mean velocity profile. Indeed, the roughness length z_0 was prescribed to 10 cm leading to an effective roughness length z_0^e of about 3 cm (see appendix A) to be compared to the 4 cm computed from the sonic anemometer measurements (Drobinski et al. 2004). The length of the steady LES is 7000 s.[1] The effective surface roughness leads to $u_* = 0.42 \text{ m s}^{-1}$, which is close to the value derived from the sonic anemometer measurements (about 0.4 m s^{-1}; Drobinski et al. 2004). Figure 2 shows a relatively deep logarithmic surface wind profile formed with no veering up to 40 m and a constant potential temperature profile, in agreement with the observations (Fig. 2). The comparison of the Monin–Obukhov stability functions ϕ_m and ϕ_h, which is a much

---

[1] The LES steadiness is reached as follows: the LES resolution was refined from 50 m down to 25, 12.50, and 6.25 m. The first LES (50-m resolution) was run during 132 000 s. The simulated fields were used as initial conditions of the finer LES (25 m). The second LES was run during 144 000 s. The same approach was used for the next two LESs. The third LES was run during 7200 s. The last LES was run during 7000 s (500 s for convergence and 6500 s to compute the statistics that are shown in the paper). The LES refinement approach allows us to have a steady simulation without using too much computation time

more demanding test for the LES, is also plotted in the bottom panels. The Monin–Obukhov stability functions ϕ_m and ϕ_h represent nondimensional gradients of wind shear and temperature and are defined such that

$$\left[\left(\frac{\partial \tilde{u}_i}{\partial z}\right)^2\right]^{1/2} = \frac{u_*}{k_0 z}\,\phi_m \qquad (3)$$

$$\left(\frac{\partial \theta}{\partial z}\right) = \frac{\theta_*}{k_0 z}\,\phi_h, \qquad (4)$$

where θ is the mean potential temperature and θ_* is the temperature scale. Businger et al. (1971) and Wyngaard and Coté (1974) show that ϕ_m and ϕ_h are given by

$$\phi_m = (1 - 15z/L_{\mathrm{MO}})^{-1/4}$$

$$\phi_h = 0.74(1 - 9z/L_{\mathrm{MO}})^{-1/2} \qquad (5)$$

for unstable case and

$$\phi_m = 1 + 4.7z/L_{\mathrm{MO}}$$

$$\phi_h = 0.74 + 4.7z/L_{\mathrm{MO}} \qquad (6)$$

for stable case, where L_{MO} is the Monin–Obukhov length. Figure 2 reveals a very good agreement between the LES and the observations, except at the second level of the LES for ϕ_m. Close to the surface, the SGS contribution to the energy is expected to be larger than the resolved part. To illustrate this point, Fig. 3 shows the vertical profiles of the total normalized variances $\overline{u^2}/u_*^2$, $\overline{v^2}/u_*^2$, and $\overline{w^2}/u_*^2$, and the SGS variance [which is equal for the three wind components, see Eq. (2)], as well as the total momentum fluxes $\overline{uw}/u_*^2$ and $\overline{vw}/u_*^2$ and the SGS momentum fluxes. The contribution of the SGS model exceeds 50% of the total variance or momentum flux below 10 m height for $\overline{u^2}/u_*^2$ (it is even lower for the other wind components) and 8 m for the momentum fluxes. It is lower than 10% above about 50 m height for $\overline{u^2}/u_*^2$ and 10 m for the momentum fluxes. We can thus arbitrarily define three regions: 1) below 10 m, the LES dynamics is strongly SGS model dependent, 2) between 10 and 50 m, the LES dynamics is moderately SGS model dependent, and 3) above 50 m, the LES dynamics is very weakly SGS model dependent (see also Carlotti and Drobinski 2004). Additional LES simulations of this case were performed to check the sensitivity of our results on the SGS scheme (see appendix B). One major conclusion is that the results of all LES are very similar to each other in the regions of the PBL where the SGS scheme contribution is negligible. So the SGS model only acts locally on the PBL flow dynamics. In a more general perspective, the robustness of our results with respect to the SGS model has also been checked in the near-surface region where
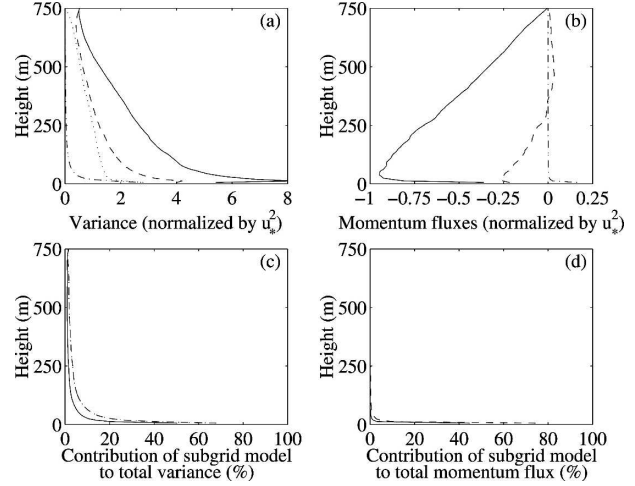

FIG. 3. (a) Vertical profile of total $\overline{u^2}/u_*^2$ (solid line), $\overline{v^2}/u_*^2$ (dashed line), $\overline{w^2}/u_*^2$ (dotted line), and of subgrid-scale variance normalized by u_*^2 (dash–dotted line). (b) Vertical profile of total $\overline{uw}/u_*^2$ (solid line), $\overline{vw}/u_*^2$ (dashed line), and of subgrid-scale momentum flux normalized by u_*^2 (dash–dotted line). (c) Vertical profile of the contribution (%) of the subgrid-scale variance to the total $\overline{u^2}$ (solid line), $\overline{v^2}$ (dashed line), and $\overline{w^2}$ (dotted line). (d) Vertical profile of the contribution (%) of the subgrid-scale momentum flux to the total $\overline{uw}$ (solid line) and $\overline{vw}$ (dashed line). The data shown in this figure are from the LES.

the SGS scheme contribution is significant (see appendix B).

3. Flow structure

a. Near-surface organized eddies

The LES flow near the ground is shown in Fig. 4, which displays cross sections parallel to the surface of the longitudinal velocity fluctuations u at various levels from 9 m up to 153 m. One has to note that in Fig. 4 and the following figures, the geographic coordinate system has been changed by a rotated coordinate system in which the x axis is aligned with the mean wind. Figure 4 shows organized regions of alternating high- and low-speed fluid aligned with the surface wind (it is also true for any one of the two other velocity components which are not shown in the horizontal cross sections). These organized large eddies in the form of near-surface streaks are ubiquitous features of LES of the PBL in which shear plays an important role in the dynamics (e.g., Deardorff 1972; Moeng and Sullivan 1994; Drobinski and Foster 2003). Streaks reside within the high-shear surface region (i.e., in the SL).

For studying the separation of the coherent structures and nonorganized turbulence, two-dimensional spectral analysis is a perfectly suited approach (Eymard
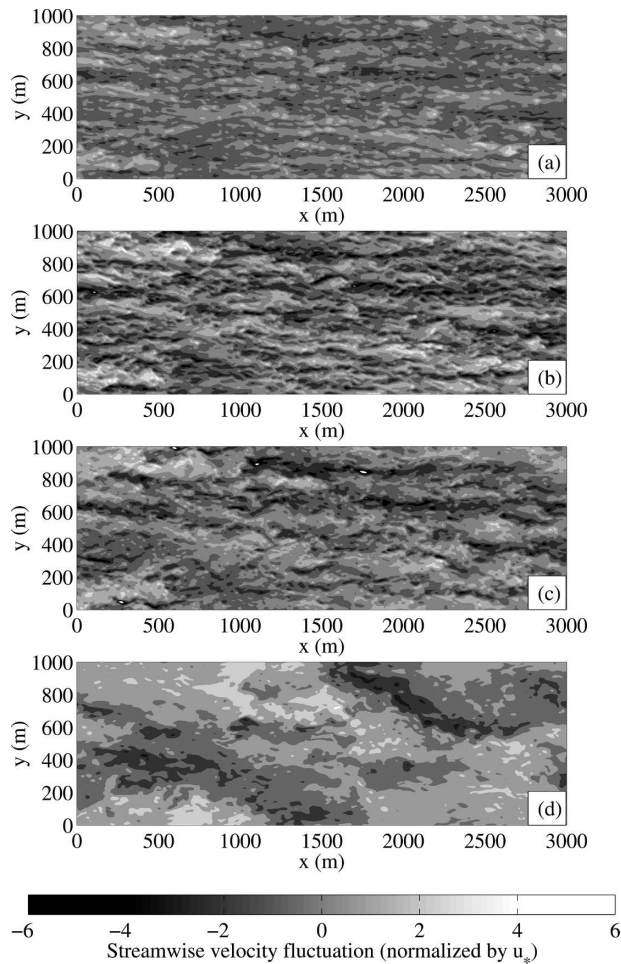
FIG. 4. Snapshot of the LES longitudinal (or streamwise) velocity fluctuation u, at (a) $z = 9$ m, (b) $z = 28$ m, (c) $z = 47$ m, and (d) $z = 153$ m. Positive u is shown in gray and negative u in white.
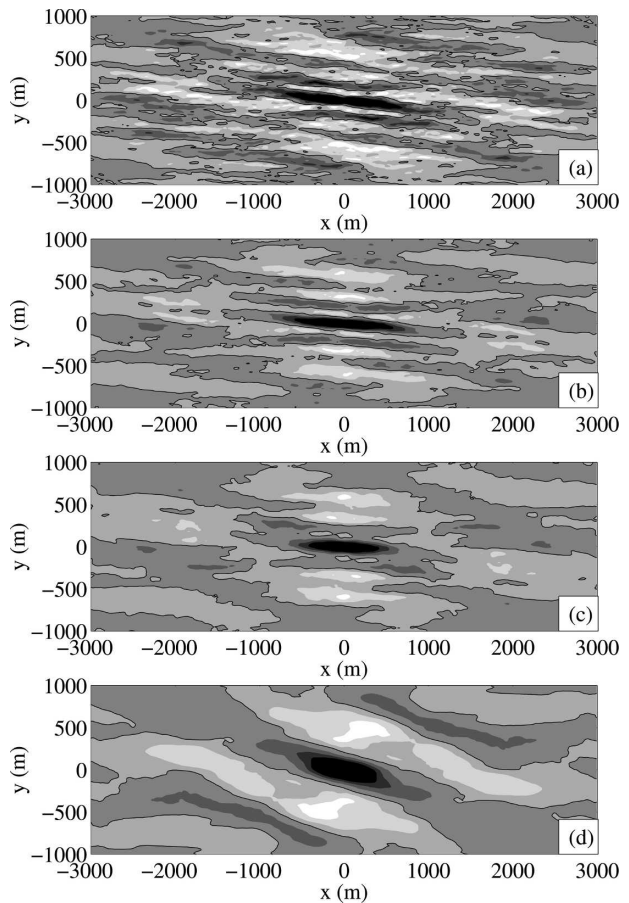

FIG. 5. Two-dimensional correlation function of the LES streamwise velocity fluctuation at (a) $z = 9$ m, (b) $z = 28$ m, (c) $z = 47$ m, and (d) $z = 153$ m. The black solid line indicates the zero-correlation. Dark (light) colors indicate positive (negative) correlation.

and Weill 1982; Drobinski et al. 1998). Figure 5 displays the two-dimensional autocorrelation function applied to the horizontal fields of the longitudinal velocity fluctuations u at the various heights shown in Fig. 4. Figure 5 shows the characteristics in terms of wavelength. The organization from the two-dimensional autocorrelation is contained in the correlation coefficients around the center. They are calculated for a small lag and as a consequence they take into account a large number of points over the horizontal field thus giving better statistical confidence. The characteristics of the structures are given by the positive and negative oscillations of the two-dimensional autocorrelation. The wavelength of the near-surface streaks is given by the distance between the negative parallel line of the central pattern. Figure 5 (as well as Fig. 4) shows that near the ground, the streak spacing is about 100 m and increases up to about 450 m at 153 m above ground level. The smaller

eddies have a 20-m vertical extent whereas the larger eddies extend up to about 150 m. The large values of the mean correlation of the central pattern at all levels indicate the atmospheric SL and the PBL are well organized. The largest structures above the SL (see bottom panel in Figs. 4 and 5) are rather reminiscent of PBL rolls and explains the slight veering of the structure orientation [the PBL rolls make an angle with the geostrophic wind direction predicted to be 18° in neutral, barotropic conditions; see Brown (1972)].

The spatial structure of the LES flow can be compared to the observations made by HRDL, which documented the radial velocity field in a plane almost parallel to the ground using a full azimuth scan at 1° elevation (the azimuth varies between 0° and 360°). To do so, a similar LES radial velocity field is computed from the LES flow using the relation between the radial velocity and the three components of the wind:

$$v_r = U \cos\phi \sin\psi + V \cos\phi \cos\psi - w \sin\phi, \quad (7)$$
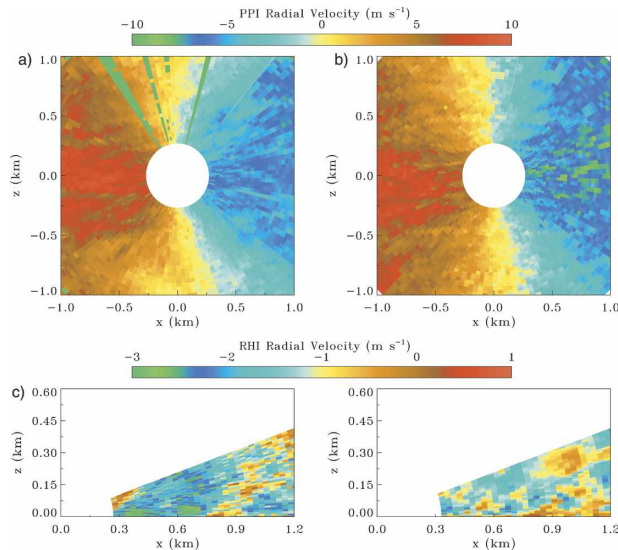
FIG. 6. (a) HRDL and (b) LES radial velocity field from full azimuth scan at 1° elevation. The height at which the laser beam is transmitted in the atmosphere is about 4 m above ground. With 1° elevation, the laser beam is at 38 m above the ground at 2 km from the lidar. Vertical cross section of (c) HRDL and (d) LES radial velocities (elevation ranged from 0° to 20°) perpendicularly to the mean surface flow. The height at which the laser beam is transmitted in the atmosphere is about 4 m above ground. Positive (negative) radial velocities correspond to air blowing away from (toward) the lidar.
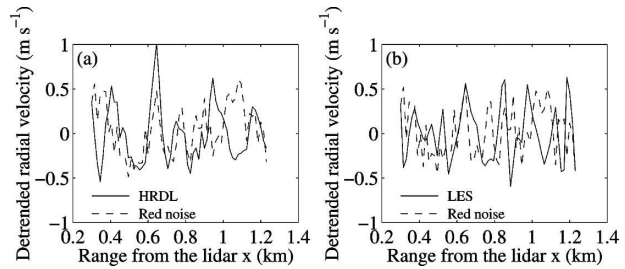

FIG. 7. (a) Observed and (b) simulated detrended radial velocity profile (solid line) at about 3 m above ground level. The dashed lines are red-noise surrogates with characteristics adapted to the measured and modeled radial velocity at that level.

where U is the zonal wind component, V the meridional wind component, w the vertical wind speed, ϕ the elevation angle, and ψ the azimuth angle. Figure 6 shows the comparison between the radial velocities from HRDL (Fig. 6a) and from Méso–NH (Fig. 6b) for the azimuth scan at $\phi = 1°$ elevation. The scans in Fig. 6a are representative of 11 scans taken over more than an hour, during which approximately along-wind streaks of about 250-m spacing were evident in each scan. Qualitatively Fig. 6b shows that the finescale structure is well captured by the LES. Both the Doppler lidar and LES flow visualization show a characteristic near-surface streak spacing of approximately 250 m oriented at about 8° from the geostrophic wind and aligned with the surface wind. From the vertical-slice scan, we can see tilted near-surface filaments extending up to about 100 m above the ground (see Figs. 6c,d). At this stage, a point by point comparison is not possible between the Doppler lidar measurements and the LES since streaks form, evolve, and decay over relatively short life times of several tens of minutes, after which they rapidly regenerate (e.g., Lin et al. 1996; Foster 1997). The flow structures observed by the Doppler lidar and the LES are thus independent realizations of the flow.

To extract and compare the dominant oscillations from the HRDL and LES data, we analyze the radial velocity profiles in the cross-wind direction obtained from the vertical-slice scan shown in Fig. 6. We first detrend the radial velocity profiles along the line-of-sight. To extract resonant modes from these series, we evaluate the power spectra of the radial velocity profile. The technique used is a conventional Blackman–Tukey correlogram of the series tapered by a 60-m-long Tukey window. To provide error bars on the spectral estimate we model the cumulative effects of measurements errors and of naturally random nonoscillatory fluctuations by a red noise. This technique is conventional when one wishes to extract oscillations from geophysical series. The choice of red noises to test the series is motivated by the fact that the null hypothesis for red-noise tests is that the series does not differ from a one-order autoregressive process, which does not contain oscillations. It also follows that all the power spectra we compute have a median shape that looks like that of a red noise in the wavelength domain we investigate. To perform the tests, we associate the series of interest with independent one-order autoregressive series whose variance and lag-1 cross correlation match those of the measured series. These one-order autoregressive series are of the form $Y_{x+dx} = aY_x + Z_x$, where Z_x is a white noise. One example of such a series is shown in Fig. 7, where it is superimposed to the measured radial velocity. These stochastic series show purely random fluctuations dominated by rather long waves, which is a classical behavior of red noises. The fact that such series can look like waves does not disprove the hypothesis that the measured wind contains oscillations, it provides a null hypothesis for what is seen. To test the robustness of spectral analysis presented next, we adopt a Monte Carlo procedure, in which spectra are compared to analyses done with ensembles of 5000 one-order autoregressive process surrogates build as described before. The results are significant if they exceed, in 99% of cases, the values obtained with the

surrogates. The power spectra of the radial velocity in the cross-wind direction average between 10- and 55-m height and between 80- and 120-m height (transverse wavenumber k_2, i.e., corresponding to the vertical-slice scan perpendicular to the mean flow) computed following Drobinski et al. (2000) approach are shown in Fig. 8. They show that the signal is dominated by oscillations with wavelengths ranging from 100 to 300 m. More precisely, for the lowest level (top panels) the significant peaks are 113, 132, 187 and 224 m whereas at the higher level (bottom panels), the peaks are 187 and 224 m. The highest peaks correspond to the near 250-m streak scale evident in the cross sections of Fig. 6. The fairly good agreement between the spectra of the measured and simulated radial velocity gives some confidence that the LES is able to capture the near-surface turbulence structure, even though in the 10–55-m height region, the impact of SGS model probably affect the intensity of the spectral peaks. In the lowest levels, the peaks at about 100-m wavelength are significant and show evidence of a multiscale structure near the surface. These smaller scales are no longer visible above 50 m, but the lower wavenumbers are present through deeper layers. At about 100-m height, the most energetic peaks have a typical wavelength of 200/300 m. The LES also shows that the large eddy scale increases linearly with height similarly to the Lin et al. (1997) numerical study. For a PBL depth of 750 m and a smooth surface, Lin et al. (1997) predict a streak scale ranging between 274 and 330 m when height increases from 5 to 35 m above ground level, which is in good agreement with the Doppler lidar and LES data (the height of the lidar line of sight lies between about 5 m and 35 m above ground level for $\phi = 1°$). Because of the limited elevation angle in the vertical-slice scans, it was not possible to make a more thorough comparison of the vertical evolution of the large-eddy scale. The spectral analysis of both the Doppler lidar and the LES data show evidence of two regions in the surface layer where different dynamical processes occur: (i) above about 50 m height in the SSL (see Figs. 8c,d), large eddies are present, with typical horizontal spacing of about 300 m and vertical extent of about 100 m. Their scale increases linearly with height (Lin et al. 1997). (ii) Below about 50 m in the ESL (see Figs. 8a,b), small eddies, with typical horizontal spacing of about 100 m (and maybe smaller, but the peaks are not significant) and vertical extent of about 50 m, coexist with the larger eddies. The smaller eddy scales do not fit with the linear relation between height and the large-eddy scales, suggesting different dynamical processes driving the large and small eddies. This behavior is consistent with Hunt and Morrison (2000) who proposed that large eddies (iden-
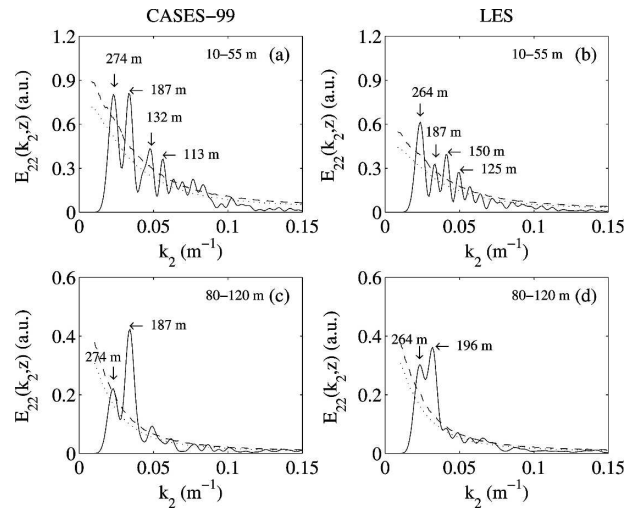

FIG. 8. Plots of $E_{22}(k_2)$ (where k_2 is the transverse wavenumber and E_{22} the transverse velocity spectrum) calculated from cross-flow HRDL vertical-slice scans are shown for two height intervals: (a), (b) 10–50 m and (c), (d) 80–120 m. The left and right columns correspond to the actual HRDL spectra and to the synthetic LES spectra. The dotted and dashed lines indicate the 95% and 99% confidence levels, respectively. The spectral resolution is $2\pi \times 9.6 \times 10^{-4}$ m^{-1}. The radial velocity profiles are detrended to remove the largest oscillations (like PBL rolls).

tified as streaks by Drobinski and Foster 2003) impinge onto the ground (top-down mechanism for eddy motion at high Reynolds number) where they generate internal boundary layers due to blocking (i.e., zero tangential velocity at the ground) in which smaller eddies [identified as cat-paws observed on water surface by Hunt and Morrison (2000); or as near-surface plumes elongated in the mean wind direction by Wilczak and Tillman (1980) and Shaw and Businger (1985)] develop. The existence of these smaller eddies is supported by the experimental work of Hommema and Adrian (2003) in the neutral PBL even though Adrian et al. (2000) disagree with Hunt and Morrison (2000) on the mechanism responsible for these substructures since they propose a bottom-up mechanism for eddy motion. There are some hints suggesting that bottom-up eddy motion theory may apply to low-to-moderate Reynolds number flows whereas top-down eddy motion theory may apply better to high Reynolds number flows, as suggested by Drobinski and Foster (2003) and Lin (2000) who found evidence for occasional downward-propagating waves from the atmospheric mixed layer into the surface region that may enhance streak growth. However, the long-lasting controversy between the top-down and bottom-up eddy motion theories is still an open question that we do not pretend to solve in this paper.

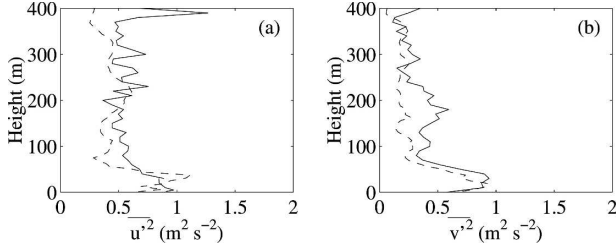The near-surface eddies contribute to significant in-

FIG. 9. Vertical profiles of the (a) longitudinal velocity variance $\overline{u'^2}$ and (b) transverse velocity variance $\overline{v'^2}$ calculated from HRDL (solid line) and LES (dashed line) vertical-slice scans.

crease in the wind velocity variance in the SL. Figure 9 displays vertical profiles of the variance of HRDL and LES radial velocities calculated from the vertical-slice scans using the procedure outlined in Banta et al. (2002). Figure 9a shows the vertical profile of the along-wind radial velocity variance $(\overline{u^2})$ and Fig. 9b shows the vertical profile of the cross-wind radial velocity variance $(\overline{v^2})$. A very good agreement is found between the data and the LES with at most 0.1 m² s⁻² bias for the longitudinal and transverse wind variances. The variance reaches a maximum between 30- and 50-m height and decreases significantly above about 80 m, especially in the cross-wind direction. This is consistent with the streaks being a major source of variation and existing at low levels in the SL. The many energetic eddies of different scales existing below about 50 m probably cause the maximum variance in the ESL.

b. Momentum transport: Quadrant analysis

Near-surface streaks occur in updraft–downdraft pairs (Moeng and Sullivan 1994; Lin et al. 1996; Foster et al. 2006). This mechanism can impact the shear production in the SL through the momentum fluxes. Indeed, Fig. 10 displays a map of the sweeps (defined as high-speed negative momentum) and ejections (low-speed negative momentum) at different heights, confirming that sweeps and ejections (black and gray areas) spread over the major part of the domain. This figure also clearly shows that the momentum pattern consists of streaky structures too.

The vertical distribution of the momentum fluxes in the LES (including the SGS term) is shown in Fig. 11. It is apparent that the mean momentum flux $\overline{uw}$ remains negative. Regions of downward (upward) vertical velocity generally coincide with regions of positive (negative) streamwise velocity fluctuations. The correlation coefficient of u and w, $\gamma_{uw} = \overline{uw}/\sqrt{\overline{u^2}\,\overline{w^2}}$, illustrates this. It is plotted as a function of height in Fig. 11, where separate contributions from updrafts and downdrafts
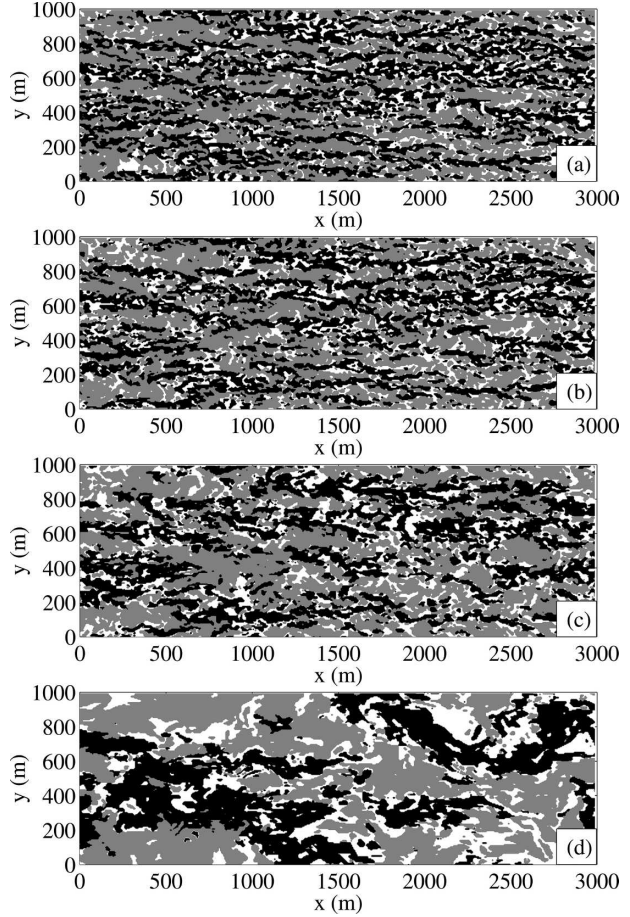

FIG. 10. The $\overline{uw}$ contributions at (a) $z = 9$ m, (b) $z = 28$ m, (c) $z = 47$ m, and (d) $z = 153$ m. Ejections $\overline{u^-w^+}$ appear in black, sweeps $\overline{u^+w^-}$ in gray, and positive contributions $\overline{u^-w^-}$ and $\overline{u^+w^+}$ in white.

are defined by averaging where $w > 0$ and $w < 0$, respectively,

$$\text{updrafts: } \gamma_{uw+} = \overline{uw}^+/\sqrt{\overline{u^2}\,\overline{w^2}}$$

$$\text{downdrafts: } \gamma_{uw-} = \overline{uw}^-/\sqrt{\overline{u^2}\,\overline{w^2}}.$$

The total correlation coefficient is shown as a solid curve, while updraft and downdraft contribution are plotted as dashed and dotted lines, respectively. Results are similar to Moeng and Sullivan (1994) S simulations (their Figs. 7–8): updraft is the dominant motion (i.e., the greater in absolute value), except very close to the ground. But the layer where the correlation coefficient is higher in downdrafts than in updrafts is contained closer to the ground here, probably because of the finer resolution [the resolution is 10.4 m in the vertical and 31.25 m in the horizontal in Moeng and Sullivan (1994)]. Following Lin et al. (1996), we can also refine
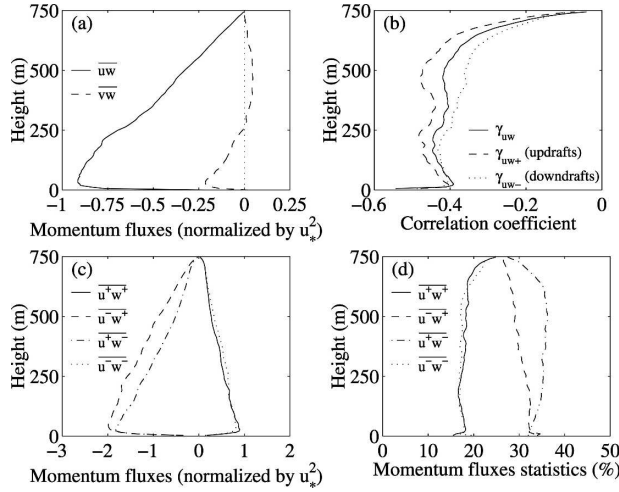
FIG. 11. (a) Momentum transport (normalized by u_*^2); (b) vertical distribution of the correlation coefficient of u and w. Dashed curve is for updrafts only, dotted curve for downdrafts only; (c) momentum fluxes (normalized by u_*^2); (d) momentum flux statistics from the LES. The terms $\overline{u^+w^+}$, $\overline{u^-w^-}$, $\overline{u^+w^-}$, (sweeps) and $\overline{u^-w^+}$, (ejections) are displayed with solid line, dotted line, dash-dotted line, and dashed line, respectively.

FIG. 12. (a), (b) Momentum flux statistics and (c), (d) momentum fluxes normalized by u_*^2 computed from (left) the CASES-99 data and (right) from the LES outputs. The terms $\overline{u^+w^+}$, $\overline{u^-w^-}$, $\overline{u^+w^-}$ (sweeps), and $\overline{u^-w^+}$ (ejections) are displayed with solid line, dotted line, dash-dotted line, and dashed line, respectively.

this by considering the four contributions to the momentum transport (quadrant analysis depending on the sign of the fluctuating velocity components u and w). Sweep and ejection events are related respectively to high- and low-speed negative momentum:

$$\overline{uw} = (\overline{u^+w^+} + \overline{u^-w^-}) + \underbrace{\overline{u^+w^-}}_{\text{sweeps}} + \underbrace{\overline{u^-w^+}}_{\text{ejections}}.$$

Where the superscripts $^+$ and $^-$ indicate the sign of the velocity fluctuation component. Negative contributions—that is, sweeps and ejections—occur in the major part of the domain (representing together in average about 65% of the domain), and have the strongest magnitude throughout the whole PBL. The vertical profiles of the resolved momentum fluxes reach a maximum in the SL at about 40 m height.

In this paper, the aim of the quadrant analysis is twofold: (i) the difference between the ESL and SSL and (ii) the comparison of the LES quadrant analysis with the quadrant analysis conducted on the measured fluxes at different height (such a comparison on the vertical with such precision has never been published to the authors' knowledge). Indeed, the eight sonic anemometers and the LES allow investigation of the vertical structure of the momentum flux $\overline{uw}$ in the region close to the surface (below 60 m). Figure 12 zooms in on the first few tens of meters in the SL and compares the simulated momentum fluxes (quadrant analysis) and statistics with the observed ones.
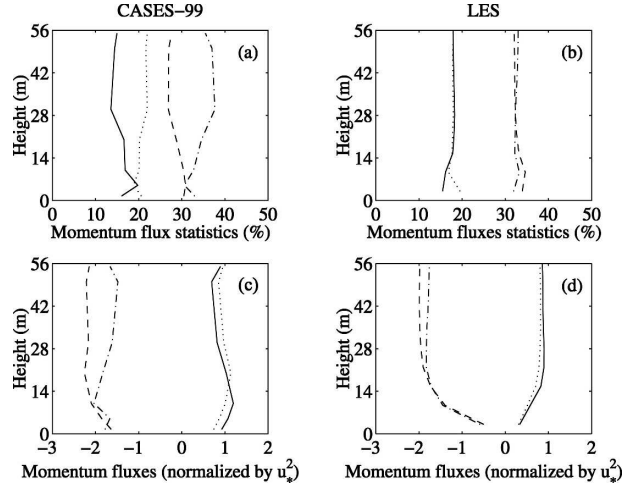
Above about 20-m height, the LES shows that sweep

$(\overline{u^+w^-})$ and ejection $(\overline{u^-w^+})$ events have the same probability of occurrence (32% each term, 64% in total) and occur more often than the positive terms $(\overline{u^+w^+}$ and $\overline{u^-w^-}$; 18% each term, 36% in total). This region of the SL corresponds to the SSL as defined by Drobinski et al. (2004). The positive terms have the same magnitude ($0.8u_*^2$), whereas the absolute magnitude of ejections is the strongest ($2u_*^2$), similarly to Lin et al. (1996) and Högström and Bergström (1996); the magnitude of the sweep events ($1.7u_*^2$) is slightly smaller than that of the ejections. The comparison with the measurements is very encouraging despite some differences, most probably due to sampling issues (the $\overline{uw}$ terms are computed in the streamwise direction and there is no perfect stationarity of the atmospheric conditions). The probability of occurrence of the quadrant terms computed from the measurements of $\overline{uw}$ by the eight sonic anemometers shows that on average the positive and negative momentum fluxes have a 36% and 64% probability of occurrence, which is the same as the LES results. However, looking at each individual term in detail, we note that the ejections occur less often than the sweeps (about 27% versus 37%) and that the $\overline{u^+w^+}$ events occur less often than the $\overline{u^-w^-}$ events (about 15% versus 21%). The magnitude of the quadrant terms shows a better agreement between the data and the LES. The positive terms have the same magnitude (between $0.9u_*^2$ and u_*^2) whereas the ejections and the sweeps have a respective absolute magnitude of $2u_*^2$ and $1.5u_*^2$. Despite the smaller occurrence of ejections in the measurements, in summation ejections transport more momentum than sweeps.

Below about 20-m height, the quantitative agreement deteriorates due to the resolution of the LES (only 3–4 points to investigate the ESL) and to the SGS parameterization induced dissipation. This region of the SL corresponds to the ESL as defined by Hunt and Carlotti (2001). All the quadrant terms from both experimental data and LES decrease in magnitude as the altitude decreases, but the decrease is sharper in the LES due to the SGS model. The magnitude of sweep and ejections are similar in the highest part of the ESL whereas they are underestimated in the very near-surface region by the LES: in the experimental data, the absolute magnitude of sweep and ejections increases from $1.7u_*^2$ at 1.5 m up to $2u_*^2$ at 10 m; in the LES, the absolute magnitude of sweep and ejections increase from $0.5u_*^2$ at 6.25 m up to $1.8u_*^2$ at 15 m. A more striking similarity between the measurements and the LES is on the occurrence of ejections that increases in the ESL, and the ejections and sweeps have a similar probability of occurrence (about 30% in the experimental data, and about 32%–35% in the LES). This could be a consequence of the link between sweeps and ejections suggested by Lin et al. (1996): sweeps impinging on the ground could be the source of (weaker) sweep-induced ejections. Or, this could point out the effect of substructures imbedded within larger structures (i.e., the streaks) as shown in Fig. 8 (see also Hunt and Carlotti 2001; Hommema and Adrian 2003). However, we may still have too few grid points in this critical layer, very close to the ground, to discuss the discrepancies in the quantitative comparison between the measured and simulated momentum fluxes within the ESL below about 20 m.

4. Spectra and variances

a. Spectra

It is recognized that turbulent eddy motion in the PBL exhibits three spectral regions (see e.g., Kaimal and Finnigan 1994): (i) the energy containing range (or large-scale turbulence), in which turbulent kinetic energy (TKE) is produced, (ii) the inertial subrange (or small-scale turbulence), in which TKE is neither produced nor dissipated, but is simply transported from large to small scales, and (iii) the dissipation range, where TKE is converted to internal energy by the action of fluid viscosity. While much effort has been devoted to investigating the inertial subrange following the success of Kolmogorov's (1941) theory ($-5/3$ power-law spectral signature), less attention was devoted to the spectral characteristics of the energy containing range despite their importance in mass, energy, and momentum transport. Indeed, the analysis of large-

scale turbulence, corresponding typically to the near-surface streak scales discussed in the previous section, is a far more complex task than that of describing the inertial or dissipation scales because of their strong anisotropy and their dependence on the flow domain boundary properties. Despite the complexity associated with analysis of large-scale turbulence, several laboratory and field experiments in Table 1 reported well defined -1 power laws at production scales for the longitudinal velocity spectrum in the SL of many boundary layer flows, including atmospheric SL (from stably to slightly unstably stratified PBL; see Lauren et al. 1999; Högström et al. 2002; Drobinski et al. 2002, 2004). However some authors (Claussen 1985; Raupach et al. 1991; Antonia and Raupach 1993) suggest that the existence and onset of the -1 power law in the atmospheric SL remains uncertain probably because of the absence of a -1 power law in the measured velocity spectra from the Kansas (see Kaimal et al. 1972) and Minnesota experiments (see Kaimal 1978). The possibility that energy containing scales, governed by the dynamics of anisotropic eddy motion and possibly boundary roughness conditions attain a universal power law in the SL is thus still the subject of ongoing researches.

Indeed, Drobinski et al. (2004) proposed recently that the near-neutral SL can be divided into three sublayers: the ESL, which is the lower sublayer where blocking of impinging eddies is the dominating mechanism and where the longitudinal velocity fluctuation spectrum E_{11} displays a k_1^{-1} intermediate spectral subrange (k_1 is the longitudinal wavenumber); the SSL, which is an intermediate sublayer, where shear affects the isotropy of turbulence and where E_{11} and E_{33} (vertical velocity spectrum) have the same spectral shape with a k_1^{-1} subrange; the upper surface layer (USL) at the upper part of the SL is suggested by Yaglom (1991), where the mean velocity profile is logarithmic and the horizontal and vertical spectra decay as $k_1^{-5/3}$. Investigating if we can find the same behavior in the present LES, and following a wavenumber range where $E_{ii} \sim k^{-1}$ with height could thus be a way to find out the extent of the ESL and SSL. Figures 13a–f display the measured and simulated $k_1 E_{11}$ and $k_1 E_{33}$ at several heights. The sonic anemometers measure the wind velocity fluctuation as a function of time. The spectra are thus function of the frequency f. The spectra are converted in spatial space using Taylor's hypothesis (we confirmed beforehand its applicability by checking that the variances of the wind velocity fluctuations are much smaller than the wind speed at the corresponding level). The frequency f is converted to k_1 using the

TABLE 1. Sample studies reporting the occurrence of a -1 power law in the longitudinal (E_{11}) and/or vertical (E_{33}) velocity at low wavenumbers ($k_1 z < 1$). This table is adapted and completed from that shown in Katul and Chu (1998).

Authors	Flow type	Comments
Tchen (1953, 1954)	Theoretical	Approximate asymptotic solution to the spectral budget based on Heisenberg's (1948) turbulent viscosity model.
Klebanoff (1954)	Flat plate boundary layer with zero-pressure gradient	-1 power law existed for $z/h = 0.05$ but not for $z/h = 0.001$ and 0.8.
Hinze (1959)	Data from Klebanoff (1954)	-1 power law occurs in regions of strong TKE production.
Pond et al. (1966)	Atmospheric SL spectra over ocean surfaces	-1 power law existed at low wavenumbers.
Bremhorst and Bullock (1970)	Fully developed pipe flow	-1 power law existed at wavenumbers equal to or greater than the pipe diameter.
Panchev (1971)	Theoretical	Prediction based on Tchen's (1953) spectral budget.
Bremhorst and Walker (1973)	Fully developed pipe flow	-1 power law noted in the inner region higher frequencies responsible for the transfer of momentum from the wall into the fluid while lower frequencies contribute to the transfer of momentum from the fluid to the wall.
Perry and Abell (1975, 1977)	Turbulent airflow in a pipe (rough and smooth walls)	-1 power law existed at low wavenumbers in the inner region. No -1 power law was measured for E_{33}.
Korotkov (1976)	Channel flow measurements	Same as above.
Bullock et al. (1978)	Fully developed pipe flow	-1 power law in the inner region for z^+ ($= z u_* / \eta$) between 70 and 500.
Hunt and Joubert (1979)	Smooth-wall duct flow	-1 power law for $k_1 z < 1$ in the logarithmic region. Townsend's (1976) attached eddy hypothesis is used for interpretation.
Kader and Yaglom (1984, 1990, 1991)	SL turbulence	-1 power law derived from dimensional analysis and height invariance of E_{ii}. Validation with data on a 40-m tower.
Perry et al. (1986)	Smooth pipe and vortex model	-1 power law observed for $z/h < 0.01$ and $k_1 z > 1$ in E_{11} but not in E_{33}.
Perry et al. (1987)	Smooth and rough boundary layers with zero-pressure gradient	-1 power law in E_{11} for both rough and smooth in the overlap region between the inner and outer flow.
Turan et al. (1987)	Fully developed pipe flow	-1 power law for $k_1 z < 1$ for pipe-flow boundary layer for zero pressure gradient.
Erm et al. (1987)	Smooth flat surface with zero-pressure gradient	Results similar to Perry et al. (1987) but with Reynolds number lower by a factor of 8.
Perry and Li (1990)	Smooth and rough boundary layers with zero-pressure gradient	-1 power law observed in E_{11} for $k_1 z > 1$ and $z u_* / \eta$ and $z/h < 0.15$.
Erm and Joubert (1991)	Moderate Reynolds number turbulent boundary layer over a flat smooth surface with zero-pressure gradient	-1 power law observed for $z/h = 0.1$ but not at $z/h > 0.35$.
Yaglom (1994)	Review of dimensional analysis of spectra	-1 power law must exist for a neutral atmospheric SL.
Katul et al. (1995, 1996)	Dynamic sublayer of a sandy dry lakebed and a forest clearing	Same as Kader and Yaglom (1984, 1990) but also inactive eddy motion investigated using simultaneous free air static pressure and velocity measurements in the forest clearing.
Richards et al. (1997, 1999), Hoxey and Richards (1992), Hunt and Morrison (2000)	Atmospheric SL at different heights (0.115, 1.01, and 10 m) over smooth terrain	Power law at intermediate spectral range for E_{11} varying with height around -1. No -1 power law for E_{33}.
Katul and Chu (1998)	Open channel measurements and atmospheric SL	
Lauren et al. (1999)	Atmospheric SL over nearly flat terrain (very smooth topography)	Power law in E_{11} around -1 (reaching -1.35) for Richardson number larger than 0.6. The value of the spectral slope the closest to -1 is found for nonconvective case.
Hunt and Carlotti (2001)	Rapid distortion theory	The existence of a -1 power-law spectral subrange in E_{11} implies no -1 power law in E_{33} in the ESL where both blocking and shear are important.

TABLE 1. (*Continued*)

Authors	Flow type	Comments
Högström et al. (2002)	Atmospheric SL in near-neutral conditions	-1 power law in E_{11} but not in E_{33} observed between 1.6 and 30 m (ESL).
Drobinski et al. (2002)	Stable atmospheric SL measurements over flat and smooth terrain	-1 power law in E_{11} but not in E_{33} observed below 10 m. and E_{33} observed above 10 m.
Drobinski et al. (2004)	Near-neutral SL measurements at different heights: 1.5, 5 10, 20, 30, 40, 50, and 55 m over flat and smooth terrain	-1 power law in E_{11} but not in E_{33} observed below 10 m (ESL). -1 power law in E_{11} and E_{33} observed above 30 m (SSL). The -1 power law is found for $k_1 z > 1$.

relationship $k_1 = 2\pi f/U$ with U being the mean wind. For E_{11}, Figs. 13a,c show a trend toward a k_1^{-1} slope at intermediate wavenumbers at the lower levels (3.125 m, which is in the ESL and about 22 m, which is in the SSL; see Figs. 13a,d, respectively), in accordance with the experimental longitudinal spectra at 5 and 30 m height.
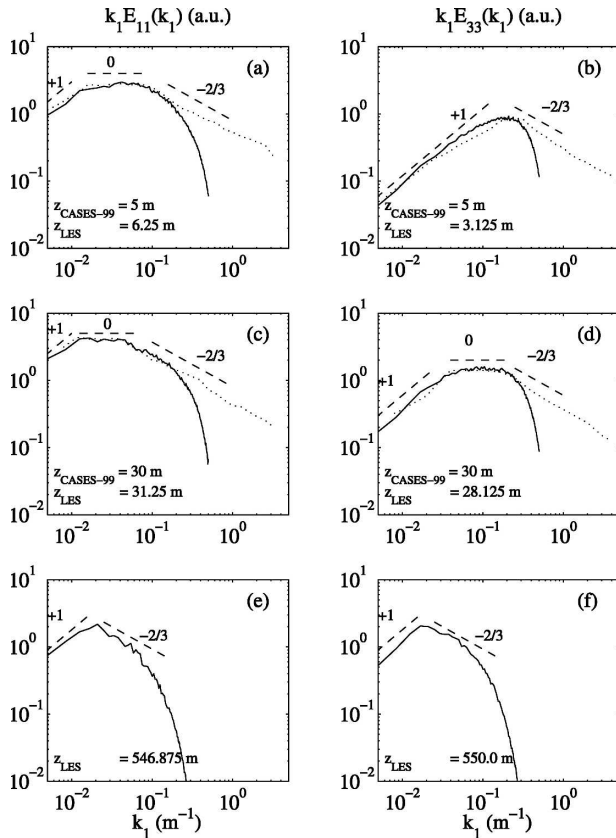

FIG. 13. Premultiplied (left) longitudinal (or streamwise) $[k_1 E_{11}(k_1)]$ and (right) vertical $[k_1 E_{33}(k_1)]$ velocity fluctuation spectra computed from the CASES-99 data (dotted line) at (top) 5-m height and (middle) at 30 m and (upper) from the LES data (solid line) at 3.125- (for E_{11}) and 6.25-m (for E_{33}) height, at (middle) 21.875- (for E_{11}) and 25-m (for E_{33}) height, and (bottom) at 546.875- (for E_{11}) and 550-m (for E_{33}) height. The dashed segments show the $-2/3$, 0 and $+1$ slopes.

The vertical profile of the estimated lower limit of the $-5/3$ range k_u for $E_{11}(k_1)$ is plotted in Fig. 14 from the measurements (circles) and the LES (squares) spectra, and both the measurements and the LES show that $k_u \sim 1/z$ for E_{11} (e.g., Kaimal et al. 1972). In the ESL below about 10 m height at 3.125 m height, the SGS model dominates the dynamics and the $-5/3$ power-law spectral subrange is very short in Fig. 13a. Because of the limited spatial resolution of the LES and because of the subgrid model (which effect is felt at wavenumbers smaller than the cutoff wavenumber) spectra are seriously damped for large wavenumbers and E_{11} has a much steeper slope compared to the measurements. Finally, Fig. 13 shows that above the SL, at about 550 m height, E_{11} does not show evidence of -1 spectral subrange, only the inertial subrange ($k_1^{-5/3}$) is visible. The reason why a -1 power-law spectral subrange exists in our experimental and numerical dataset is given by Katul and Chu (1998) who showed that when strong interaction between the mean flow and turbulent vorticity field occurs, measurements in atmospheric SL and wind tunnel, theoretical predictions by analytical solutions (Tchen 1953, 1954), or dimensional analysis (Kader and Yaglom 1990) are all in agreement and confirm the existence of a -1 power law in E_{11}. Practical methods to estimate whether the mean flow and the turbulent vorticity are strongly interacting have not
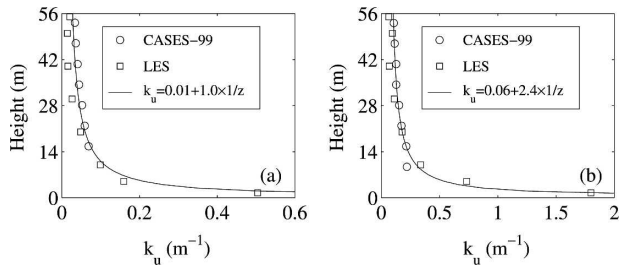

FIG. 14. Vertical profile of the lower limit of the $-5/3$ range for (a) E_{11} and (b) E_{33}. The circles and squares correspond to the measurements and the model outputs. The solid line corresponds to $k_u \simeq 1.0 \times 1/z$ for (a) E_{11} and $k_u \simeq 2.4 \times 1/z$ for (b) E_{33}.

been well developed with the exception of Panchev (1971) who suggests that

the interaction is weak if $\dfrac{\partial U}{\partial z} \ll \sqrt{\langle \omega_i \omega_i \rangle}$

the interaction is strong if $\dfrac{\partial U}{\partial z} \approx \sqrt{\langle \omega_i \omega_i \rangle}$, (8)

where $\Omega = \partial U/\partial z$ is the mean flow vorticity and $\omega_i = \varepsilon_{ijk}\partial u_k/\partial x_j$ is the fluctuating vorticity (ε_{ijk} being the alternating tensor). Equation (8) is difficult to compute from the point measurements at the main tower or from HRDL radial velocity field (one single wind component; i.e., the radial velocity, being available). The LES data allow us to compute the two vorticity terms. Figure 15 shows that the ratio $\sqrt{\langle \omega_i \omega_i \rangle}/(\partial U/\partial z)$ of turbulent to mean vorticities exceeds 10 above about 100 m, which corresponds to the SL top. Taking this value as the approximate transition between strong (below 100 m) and weak (above 100 m) interaction between the mean flow vorticity and the fluctuating vorticity, Katul and Chu (1998) show that in case of strong interaction, a -1 ($-5/3$) power law exists if the turbulent production is much larger (weaker) than turbulent energy transfer, whereas in case of weak interaction, only a $-5/3$ power law is expected. Following Tchen's (1953) analysis, the ratio of energy transfer to turbulent production is $\langle \omega_i \omega_i \rangle_k/\langle \Omega^2 \rangle_k$ where $\langle \rangle_k$ is the average over wavenumbers smaller than k. Katul and Chu (1998) approximate $\langle \omega_i \omega_i \rangle_k \approx k^2 u_*^2$, so the ratio becomes $ku_*/\Omega = ku_*/(u_*/k_0 z) = 0.4kz$. For resonance to occur between the mean and fluctuating vorticities, the ratio $0.4kz$ must be of order of unity. A direct consequence of such an order of magnitude argument is that maximum interaction between mean and turbulent vorticities occurs at scales kz of order of $1/0.4$, which is of order of unity. This is consistent with Fig. 14, which shows that the transition between production subrange (-1 power law) to inertial subrange ($-5/3$ power law) occurs at $k_u \sim 1/z$ for E_{11}, which is also the upper wavenumber limit for the -1 power law in the ESL and SSL (where the -1 power-law subrange exists). The expression of the ratio of turbulent to mean vorticities also shows that the interaction between the mean and fluctuating vorticities becomes weak for $kz \ll 1$, hence the -1 power law cannot extend to $kz \approx 0$. From the measurements and the LES, we find that for E_{11} the -1 power law ranges between about $kz \approx 0.1$ and $kz \approx 1$, which is in agreement with the overlap region between outer and inner scaling of Perry et al. (1987).

For E_{33}, Fig. 13 shows that in the SSL, a k_1^{-1} subrange is visible on E_{33} at 22 m (for the LES) in good agreement with the measurements made at 30 m, whereas
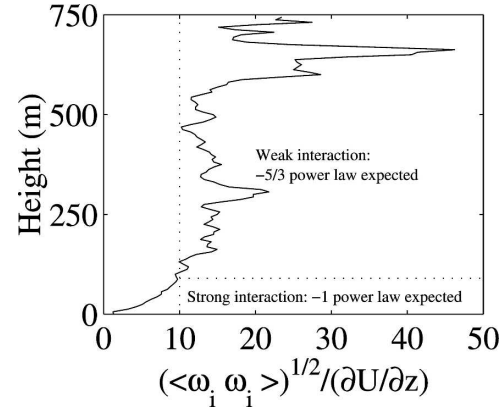

FIG. 15. Vertical profile of the ratio of turbulent to mean vorticities, $\sqrt{\langle \omega_i \omega_i \rangle}/(\partial U/\partial z)$, computed from the LES wind field.

above the SL, at about 550 m height, only the $k_1^{-5/3}$ subrange is visible. At $z = 6.25$ m, in the ESL, E_{33} does not show any -1 and $-5/3$ subranges. However, the wavenumber corresponding to the transition between the large scales ($+1$ power law) and the small scale affected by the SGS model, fits with the curve $k_u \sim 2.4/z$ shown in Fig. 14, which displays the height dependence of the lower limit of the $-5/3$ range for E_{33}. We may thus think that a -1 slope does not exist at this level for E_{33} but, because of the SGS model, it is not possible to have a more robust quantitative conclusion below 10 m in the ESL. However, one significant result is that E_{11} and E_{33} do not have the same shape in the LES similarly to the measurements and as expected by rapid distortion theory (RDT; Hunt and Carlotti 2001). When the -1 power law exists in E_{33} (i.e., above about 20 m in the LES and above 30 m in the measurements), it exists for $kz > 1$ (see Fig. 14), showing that the dimensional analysis in Kader and Yaglom (1991) is not valid for E_{33}. Katul and Parlange (1995) observed a limited -1 power law in their E_{33} spectra but for $kz > 1$ as well as Katul and Chu (1998) in the atmospheric SL despite the low-level height of their measurements. The absence of a -1 power law at $kz \ll 1$ in the E_{33} spectrum is consistent with the inactive eddy hypothesis in Perry et al. (1987). However, Katul and Chu (1998) did not find any -1 power law in their open channel experiment.

In summary, looking at all levels in the LES, Fig. 13 speaks in favor of a 20 m deep ESL (as a layer without -1 slope for E_{33}), which is consistent with Hunt and Carlotti (2001) prediction and Drobinski et al. (2004) observations. Above this height, the -1 range is observable up to about 100 m, which may be considered as an upper limit of the SSL [which is consistent with Yaglom (1991)].
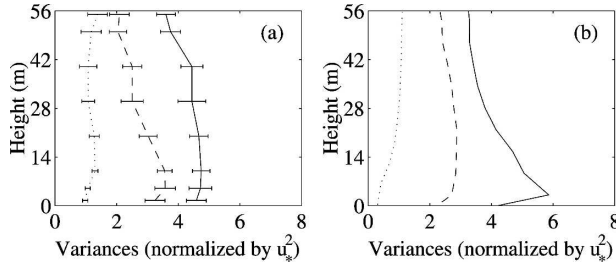
FIG. 16. Variances $\overline{u'^2}$ (solid line), $\overline{v'^2}$ (dashed line), and $\overline{w'^2}$ (dotted line) computed in the streamwise direction and normalized by u_*^2 from (a) the CASES-99 data and (b) from the LES. The error bars indicate the $1 - \sigma$ uncertainty.

b. Variances

The spectra $E_{11}(k_1)$, $E_{22}(k_1)$, and $E_{33}(k_1)$ are directly related to the variances $\overline{u^2}$, $\overline{v^2}$, and $\overline{w^2}$ computed in the streamwise direction, which are compatible with the time series measurements provided by the sonic anemometers. In Fig. 16, we thus compare in the SL the vertical profiles of the normalized streamwise variances $\overline{u^2}/u_*^2$, $\overline{v^2}/u_*^2$, and $\overline{w^2}/u_*^2$, from the sonic-anemometer measurements and from the LES. One has to notice that $\overline{v^2}$ differs in Figs. 9b and 16: indeed, in Fig. 9b, $\overline{v^2}$ is computed in the cross-wind direction, whereas in Fig. 16 it is computed in the along-wind direction. Qualitatively, the vertical profiles of the variances display a similar shape since $\overline{u^2}/u_*^2$, $\overline{v^2}/u_*^2$, and $\overline{w^2}/u_*^2$ increase between the ground and about 10 m where they reach a maximum, then $\overline{u^2}/u_*^2$ and $\overline{v^2}/u_*^2$ decrease with height while $\overline{w^2}/u_*^2$ is roughly constant. The variances increasing with height in the lower ESL is a rather new result since similarity theory predicts a constant profile in neutral conditions (e.g., Stull 1988). To the authors' knowledge, the only existing study on the near-surface vertical profile of wind variance is by Yahaya and Frangi (2005, manuscript submitted to *J. Atmos. Sci.*) who showed experimentally and theoretically that in the vicinity of the ground (up to 4 m above ground level), the variance of the horizontal wind varies logarithmically with height. The parameters of the logarithmic function include the friction velocity and the roughness length scale.

Quantitatively, the agreement between the LES and the measurements is very good in the SSL (i.e., above about 20 m) with less than 10% deviation. The variances $\overline{u^2}/u_*^2$, $\overline{v^2}/u_*^2$, and $\overline{w^2}/u_*^2$ are about 5–6, 3, and 1–2, respectively, as also found by Panofsky (1974). The ratios of $\overline{v^2}/\overline{u^2}$ and $\overline{w^2}/\overline{v^2}$ are about 0.5, which is in good agreement with LES studies (Moeng and Sullivan 1994) and observations (Nicholls and Readings 1979; Grant 1986, 1992). It is generally stated that $\overline{w^2}$ is constant with height in the lower atmosphere (Panofsky 1974;

Yaglom 1991) and this was found in the Kansas experiments. Kader and Yaglom (1991) and Yaglom (1991) also show that a -1 intermediate subrange in E_{11}, E_{22}, and E_{33} (i.e., in the SSL) leads to variances or spectra independent of height. This agrees with the data analyzed in the present paper, where $\overline{w^2} \simeq 1.5u_*^2$ above 20 m in the SSL.

Similar to the comparison of momentum fluxes, the coarse vertical resolution of the LES affects the performance of the comparison in the ESL. Below about 20 m, simulated $\overline{v^2}/u_*^2$ and $\overline{w^2}/u_*^2$ have lower values than the observations: averaging between the ground and 20 m height, $\overline{v^2}/u_*^2$ is equal to about 2.7 in the LES versus 3.4 in the measurements; $\overline{w^2}/u_*^2$ is equal to about 0.6 in the LES versus about 1 in the measurements. On the contrary, $\overline{u^2}/u_*^2$ is slightly overestimated in the LES and is equal to about 5.2 versus 4.7 in the measurements. Despite these discrepancies, a very interesting point is the simulated vertical profile of $\overline{w^2}/u_*^2$ ESL, which increases from 0.5 at 6.25 m height to 1 at 20 m height. Even underestimated, this evolution is consistent with the measurements and previous experiments like the 1972 Minnesota experiments when $\overline{w^2}$ was found to increase by 13% between 4 and 16 m. These latter observations are consistent with wind-tunnel boundary layer data (e.g., Mulhearn and Finnigan 1978; Ferrero and Racca 2004). Högström (1990) also measured an increase of $\overline{w^2}/u_*^2$ from about u_*^2 to about $1.5u_*^2$ for heights up to about 0.04 h. Hunt and Carlotti (2001) were able to explain the increase of vertical velocity variances and to propose that $\overline{w^2}$ scales as $z^{2/3}$: Drobinski et al. (2004) found that $\overline{w^2} = 0.16 + 0.017z^{2/3}$ was a good fit for $\overline{w^2}$ measured with the sonic anemometers; for the LES, the best fit is $\overline{w^2} = 0.03 + 0.017z^{2/3}$, which reflects the negative bias of the LES with respect to the observations due to the SGS model.

5. Conclusions

We have performed a thorough quantitative validation of an LES of a neutrally stratified SL using sonic anemometers and one Doppler lidar, which proved to be appropriate instruments for LES validation. The combined use of the experimental database and the numerical simulations allow to complete the vision of the shear-driven SL dynamics, first sketched by Hunt and Carlotti (2001) and Drobinski et al. (2004). In particular this study shows evidence of the multiscale nature of the neutral SL. It is consistent with theories predicting that the primary mechanism of eddy motion in high Reynolds number wall layers is top-down, but this consistency does not prove the top-down eddy mo-

tion theory. There is no overwhelming evidence to support this in this manuscript and more work is needed to put some light on the controversy between the top-down and bottom-up eddy motion theories.

This study confirms the results obtained in previous studies that a -1 power-law spectral subrange exits in the longitudinal velocity fluctuation spectra in the SL and proves the capability of LES to reproduce this spectral feature. If the subgrid model can affect the result in the ESL, the SSL is weakly dependent on the subgrid model, which thus gives quantitative confidence in the LES. Computing the mean and fluctuating vorticities from the LES data, we could explain the cause of the -1 power-law existence in our CASES-99 and LES datasets. Indeed, we found strong (weak) interaction between the mean flow and turbulent vorticity below (above) about 100 m. Katul and Chu (1998), based on Tchen's (1953) and Kader and Yaglom's (1991) works, showed that in case of weak interaction, only a $-5/3$ power law is expected in the spectra, which is consistent with the LES spectra. Similarly they showed, that in case of strong interaction, a -1 ($-5/3$) power law exists if the turbulent production is much larger (weaker) than turbulent energy transfer. We found that for $k_1 z > 1$ ($k_1 z < 1$), turbulent production is larger (weaker) than turbulent energy transfer, which is consistent with -1 ($-5/3$) power-law existence. So, using the LES, we put some light on the origin of the -1 power-law existence in our CASES-99 dataset.

This study finally shows the different nature of turbulence in the ESL and SSL from a spectral point of view and second-order moment statistics. One has to note that good quantitative agreement is found between the LES and the measurements in the SSL, while near the surface in the ESL, because of the small number of grid points and the subgrid-scale model, only qualitative similarity is found between the measurements and the LES, which however indicates that the LES captures at least part of the physics of the ESL. We found that in the vertical velocity spectra, the absence of a -1 power law in the ESL is strongly suggested but higher resolution would be needed to raise any ambiguity. In the SSL, the -1 power law is observable from about 20 m, which corresponds to the ESL depth, up to about 100 m, which corresponds to the SSL top height. The vertical profiles of velocity variances and momentum fluxes show that in the ESL, both the measurements and the LES show that $\overline{w^2}$ scales as $z^{2/3}$ whereas it is constant within the SSL. Concerning the momentum transport, ejections are found to contribute identically to the momentum flux as do sweeps in the ESL, whereas in the SSL ejections are more energetic.

APPENDIX A

On the Influence of the Cuxart et al. Subgrid Model on the Effective Value of z_0

Two error sources can affect the effective value of the effective z_0, namely the truncation effect (which is crucial near the surface due to the log law) and the SGS. In the surface layer, $U = (u_*/\kappa) \ln(z/z_0)$, and therefore, writing z_0 as the apparent roughness at height $\Delta/2$ and z_0^e the apparent roughness at height $3\Delta/2$,

$$\ln \frac{z_0^e}{z_0} = \ln 3 - \frac{\kappa}{u_*} [U(3\Delta/2) - U(\Delta/2)]. \quad \text{(A1)}$$

On the other hand, according to the subgrid model,

$$\begin{cases} -\overline{uw} = \mathcal{L}_K E^{1/2} \dfrac{dU}{dz} \\ \varepsilon = \dfrac{E^{3/2}}{\mathcal{L}_\varepsilon} \end{cases} \quad \text{(A2)}$$

where

$$\begin{cases} \mathcal{L}_K = C_K L \\ \mathcal{L}_\varepsilon = \dfrac{L}{C_\varepsilon} \end{cases} \quad \text{(A3)}$$

and the TKE equation reduces to a balance of dissipation with production by shear:

$$\varepsilon = -\overline{uw}\,\frac{dU}{dz}\,. \qquad (A4)$$

It follows from these subgrid model considerations that

$$\frac{dU}{dz} = \frac{u_*}{\mathcal{L}_K^{3/2}\,\mathcal{L}_\varepsilon^{1/2}}\,. \qquad (A5)$$

Hence

$$U(3\Delta/2) - U(\Delta/2) \approx \Delta\,\frac{dU}{dz} + \underbrace{\frac{\Delta^2}{2}\,\frac{d^2U}{dz^2} + \frac{\Delta^3}{6}\,\frac{d^3U}{dz^3} + \cdots}_{err}.$$

$$(A6)$$

Putting Eqs. (A5) and (A6) in Eq. (A1), it follows

$$\ln\frac{z_0^e}{z_0} \approx \ln3 - \kappa\,\frac{\Delta}{L}\,\frac{C_\varepsilon^{1/4}}{C_K^{3/4}} - \frac{\kappa}{u_*}\,err(z = \Delta); \qquad (A7)$$

that is for $L = \Delta$, $C_\varepsilon = 0.7$ and $C_K = 0.066$,

$$z_0^e \approx 0.3 z_0 \qquad (A8)$$

so that for $z_0 = 10$ cm, $z_0^e \approx 3$ cm.

APPENDIX B

On the Influence of the Subgrid Model on the LES Results near the Ground

In this paper, we present a numerical analysis of the SL using LES. Near the ground, the results may be sensitive to the SGS turbulent scheme. A sensitivity analysis of the LES results to different SGS schemes was thus conducted in order to check their robustness. Two additional large-eddy simulations of the present case were performed with different SGS schemes using a roughness length $z_0 = 3$ cm: (i) Cuxart et al. (2000) SGS scheme with Redelsperger et al. (2001) modified mixing length to account for near-surface turbulence anisotropy (in this case, the SGS model does not affect the roughness length since from appendix A, it can easily be shown that when $z_0 = 3$ cm, $z_0^e \approx 3$ cm); (ii) the Smagorinsky (1963) SGS scheme of lower order (without prognostic TKE) widely used in fluid mechanics.

A relatively basic formulation of the Smagorinsky scheme is used here. The turbulent stresses are defined as:

$$\tau_{ij} - \frac{1}{3}\,\delta_{ij} = -2\nu_T S_{ij} \quad \text{with} \quad S_{ij} = \frac{1}{2}\left(\frac{\partial u_i}{\partial x_j} + \frac{\partial u_j}{\partial x_i}\right),$$

where the turbulent viscosity is taken as (with $C = 0.17$):
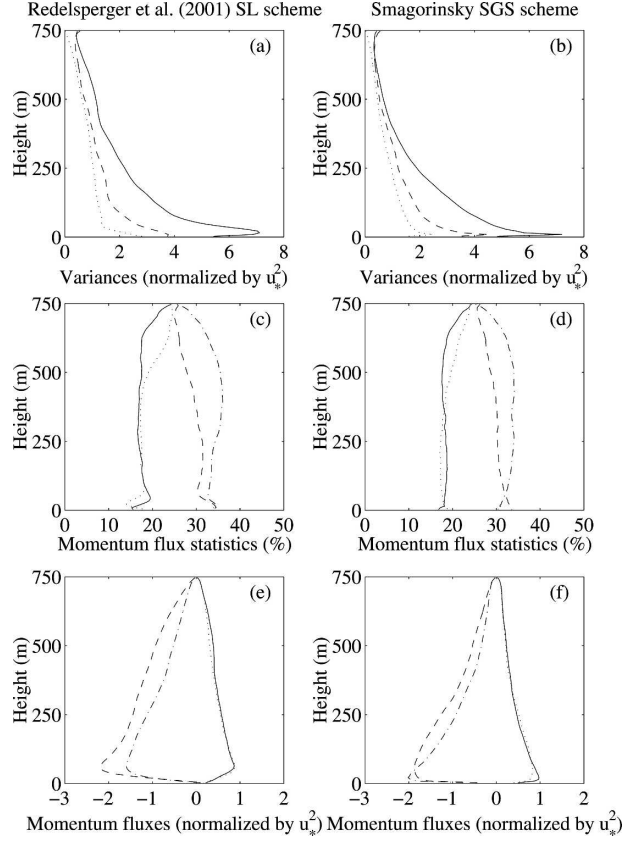
$$\nu_T = (CL)^2 (2S_{ij}S_{ij})^{1/2}.$$

FIG. B1. Variances (a), (b) $\overline{u^2}/u_*^2$ (solid line), $\overline{v^2}/u_*^2$ (dashed line), $\overline{w^2}/u_*^2$ (dotted line); (c), (d) momentum flux statistics from the LES. (e), (f) Momentum fluxes (normalized by u_*^2), the terms $\overline{u^+w^+}$, $\overline{u^-w^-}$, $\overline{u^+w^-}$ (sweeps) and $\overline{u^-w^+}$ (ejections) are displayed with solid line, dotted line, dash–dotted line, and dashed line, respectively. The results obtained (left) with Cuxart et al. (2000) SGS using Redelsperger et al. (2001) modified mixing length and (right) with Smagorinsky SGS scheme.

To take into account the SL, L is defined as follows:

$$\frac{1}{(CL)^2} = \frac{1}{(C\Delta)^2} + \frac{1}{(\kappa z)^2}\,.$$

The resolved LES turbulent quantities (variances and momentum fluxes) from all simulations (e.g., variances in Figs. B1a,b and those of the reference simulation corresponding to Fig. 3a; momentum fluxes in Figs. B1c–f, and those of the reference simulation corresponding to Figs. 11c,d), are similar over the whole PBL depth. The negligible sensitivity of our results on the SGS scheme in the PBL suggests that the SGS schemes impact locally the PBL dynamics, but not in the region of the PBL where, the SGS contribution is negligible.

The TKE Cuxart scheme with the standard mixing length Δ (Δ being the mesh size of the simulation) and
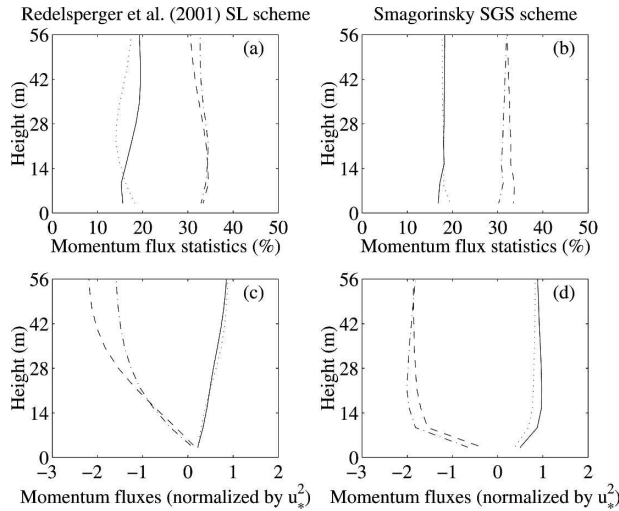
FIG. B2. Same as Figs. B1c–f zoomed on the first 56 m.

the Smagorinsky scheme have similar contributions near the ground (below 30 m) so the flow structure and turbulent statistics (variances and fluxes) are very similar for the two corresponding LES, even in the ESL (e.g., Figs. B2b,d and 12b,d). When Redelsperger et al. (2001) modified mixing length is used (which accounts for anisotropic turbulence in the SL), the SGS scheme contribution is larger, thus contributing to smooth the LES flow. Nevertheless, the results from this LES are still consistent with the two other LES using the standard Cuxart et al. (2000) and Smagorinsky SGS schemes (Figs. B2a,c): even if the absolute values of the resolved momentum fluxes retrieved from the LES, which uses Redelsperger et al. (2001) modified mixing length are smaller than those obtained from the LES, which use the standard Cuxart et al. (2000) and Smagorinsky SGS schemes, the relative contributions of the four momentum flux components [$\overline{u^+w^+}$, $\overline{u^-w^-}$, $\overline{u^+w^-}$ (sweeps) and $\overline{u^-w^+}$ (ejections)] remain unchanged. As a conclusion, the results of the three LES using different SGS schemes are all similar to our experimental data (with their own accuracy). By using in synergy the results from the observations and the LES, this paper thus allows the improvement of our understanding on the physics of the SL.

REFERENCES

Adrian, R. J., C. D. Meinhart, and C. D. Tomkins, 2000: Vortex organisation in the outer region of the turbulent boundary layer. *J. Fluid Mech.,* **422,** 1–54.

Andren, A., A. R. Brown, J. Graf, P. J. Mason, C. H. Moeng, F. T. M. Nieuwstadt, and U. Schumann, 1994: Large-eddy simulation of a neutrally stratified boundary layer: A comparison of four computer codes. *Quart. J. Roy. Meteor. Soc.,* **120,** 1457–1484.

Antonia, R. A., and M. R. Raupach, 1993: Spectral scaling laws in a high Reynolds number laboratory boundary layer. *Bound.-Layer Meteor.,* **65,** 289–306.

Avissar, R., E. W. Eloranta, K. Gürer, and G. J. Tripoli, 1998: An evaluation of the large-eddy simulation option of the regional atmospheric modeling system in simulating a convective boundary layer: A FIFE case study. *J. Atmos. Sci.,* **55,** 1109–1130.

Banta, R. M., R. K. Newsom, J. K. Lundquist, Y. L. Pichugina, R. L. Coulter, and L. Mahrt, 2002: Nocturnal low-level jet characteristics over Kansas during CASES-99. *Bound.-Layer Meteor.,* **105,** 221–252.

——, Y. L. Pichugina, and R. K. Newsom, 2003: Relationship between low-level jet properties and turbulence kinetic energy in the nocturnal stable boundary layer. *J. Atmos. Sci.,* **60,** 2549–2555.

Bremhorst, K., and K. J. Bullock, 1970: Spectral measurements of temperature and longitudinal velocity fluctuations in fully developed pipe flow. *Int. J. Heat Mass Transfer,* **13,** 1313–1329.

——, and T. B. Walker, 1973: Spectral measurements of turbulent momentum transfer in fully developed pipe flow. *J. Fluid Mech.,* **61,** 173–186.

Brown, R. A., 1972: On the inflection point instability of a stratified Ekman boundary layer. *J. Atmos. Sci.,* **29,** 850–859.

Bullock, K. J., R. E. Cooper, and F. H. Abernathy, 1978: Structural similarity in radial correlations and spectra of longitudinal velocity fluctuations in pipe flow. *J. Fluid Mech.,* **88,** 585–608.

Businger, J. A., J. C. Wyngaard, Y. Izumi, and E. F. Bradley, 1971: Flux–profile relationships in the atmospheric surface layer. *J. Atmos. Sci.,* **28,** 181–189.

Carlotti, P., 2002: Two point properties of atmospheric turbulence very close to the ground: Comparison of a high resolution LES with theoretical models. *Bound.-Layer Meteor.,* **104,** 381–410.

——, and P. Drobinski, 2004: Length-scales in wall-bounded high Reynolds number turbulence. *J. Fluid Mech.,* **516,** 239–264.

Claussen, M., 1985: A model of turbulence spectra in the atmospheric surface layer. *Bound.-Layer Meteor.,* **33,** 151–172.

Cuxart, J., P. Bougeault, and J. L. Redelsperger, 2000: A multiscale turbulence scheme apt for LES and mesoscale modeling. *Quart. J. Roy. Meteor. Soc.,* **126,** 1–30.

Deardorff, J. W., 1972: Numerical investigation of neutral and unstable planetary boundary layers. *J. Atmos. Sci.,* **29,** 91–115.

——, 1980: Stratocumulus-capped mixed layers derived from a three-dimensional model. *Bound.-Layer Meteor.,* **18,** 495–527.

Drobinski, P., and R. C. Foster, 2003: On the origin of near-surface streaks in the neutrally-stratified planetary boundary layer. *Bound.-Layer Meteor.,* **108,** 247–256.

——, R. A. Brown, P. H. Flamant, and J. Pelon, 1998: Evidence of organized large eddies by ground-based Doppler lidar, sonic anemometer and sodar. *Bound.-Layer Meteor.,* **88,** 343–361.

——, A. M. Dabas, and P. H. Flamant, 2000: Remote measurement of turbulent wind spectra by heterodyne Doppler lidar technique. *J. Appl. Meteor.,* **39,** 2434–2451.

——, R. K. Newsom, R. M. Banta, P. Carlotti, R. C. Foster, P. Naveau, and J. L. Redelsperger, 2002: Turbulence in a shear-driven nocturnal surface layer during the CASES-99 experiment. Preprints, *15th Symp. on Boundary Layers and Turbulence,* Wageningen, Netherlands, Amer. Meteor. Soc., P3.8.

——, P. Carlotti, R. K. Newsom, R. M. Banta, R. C. Foster, and

J. L. Redelsperger, 2004: The structure of the near-neutral surface layer. *J. Atmos. Sci.,* **61,** 699–714.

Erm, L. P., and P. N. Joubert, 1991: Low Reynolds number turbulent boundary layers. *J. Fluid Mech.,* **230,** 1–44.

——, A. J. Smits, and P. N. Joubert, 1987: Low Reynolds number turbulent boundary layers on a smooth flat surface in a zero pressure gradient. *Turbulent Shear Flows,* F. Durst et al., Eds., Vol. 5, Springer-Verlag, 186–196.

Eymard, L., and A. Weill, 1982: Investigation of clear air convective structures in the PBL using a dual Doppler radar and a Doppler sodar. *J. Appl. Meteor.,* **21,** 1891–1906.

Ferrero, E., and M. Racca, 2004: The role of the nonlocal transport in modeling the shear-driven atmospheric boundary layer. *J. Atmos. Sci.,* **61,** 1434–1445.

Foster, R. C., 1997: Structure and energetics of optimal Ekman layer perturbations. *J. Fluid Mech.,* **333,** 97–123.

——, F. Vianey, P. Drobinski, and P. Carlotti, 2006: Near-surface coherent structures and the momentum flux in a large eddy simulation of neutrally-stratified boundary layer. *Bound.- Layer Meteor.,* **120,** 229–255.

Fritts, D. C., C. Nappo, D. M. Riggin, B. B. Balsley, W. E. Eichinger, and R. K. Newsom, 2003: Analysis of ducted motions in the stable nocturnal boundary layer during CASES-99. *J. Atmos. Sci.,* **60,** 2450–2472.

Grant, A. L. M., 1986: Observations of boundary layer structure made during the 1981 KONTUR experiment. *Quart. J. Roy. Meteor. Soc.,* **112,** 825–841.

——, 1992: The structure of turbulence in the near-neutral atmospheric boundary layer. *J. Atmos. Sci.,* **49,** 226–239.

Grund, C. J., R. M. Banta, J. L. George, J. N. Howell, M. J. Post, R. A. Richter, and A. M. Weickmann, 2001: High-resolution Doppler lidar for boundary-layer and cloud research. *J. Atmos. Oceanic Technol.,* **18,** 376–393.

Heisenberg, W., 1948: Zur statistischen theorie der turbulenz. *Z. Phys.,* **124,** 628–657.

Hinze, J. O., 1959: *Turbulence.* McGraw Hill, 586 pp.

Högström, U., 1990: Analysis of turbulence structure in the surface layer with a modified similarity theory formulation for near neutral conditions. *J. Atmos. Sci.,* **47,** 1949–1972.

——, and H. Bergström, 1996: Organized turbulence structures in the near-neutral atmospheric surface layer. *J. Atmos. Sci.,* **53,** 2452–2464.

——, J. C. R. Hunt, and A. S. Smedman, 2002: Theory and measurements for turbulence spectra and variances in the atmospheric neutral surface layer. *Bound.-Layer Meteor.,* **103,** 101–124.

Hommema, S. E., and R. J. Adrian, 2003: Packet structure of surface eddies in the atmospheric boundary layer. *Bound.-Layer Meteor.,* **106,** 35–60.

Hoxey, R. P., and P. J. Richards, 1992: Structure of the atmospheric boundary layer below 25 m and implications to wind loading on low-rise buildings. *J. Wind Eng. Ind. Aerodyn.,* **41–44,** 317–327.

Hunt, I. A., and P. N. Joubert, 1979: Effects of small streamline curvature on turbulent duct flow. *J. Fluid Mech.,* **91,** 633–659.

Hunt, J. C. R., and J. F. Morrison, 2000: Eddy structure in turbulent boundary layers. *Eur. J. Mech. Fluids,* **19,** 673–694.

——, and P. Carlotti, 2001: Statistical structure at the wall of the high Reynolds number turbulent boundary layer. *Flow Turb. Combust.,* **66,** 453–475.

Kader, B. A., and A. M. Yaglom, 1984: Turbulent structure of an unstable atmospheric layer. *Nonlinear and Turbulent Pro-*

cesses in Physics, R. Z. Sagdeyev, Ed., Vol. 2, Harwood Academic, 829–845.

——, and ——, 1990: Mean fields and fluctuation moments in unstably stratified turbulent boundary layers. *J. Fluid Mech.,* **212,** 637–662.

——, and ——, 1991: Spectral and correlation functions of surface layer turbulence in unstable thermal stratification. *Turbulence and Coherent Structures,* O. Metais and M. Lesieur, Eds., Kluwer Academic, 388–412

Kaimal, J. C., 1978: Horizontal velocity spectra in an unstable surface layer. *J. Atmos. Sci.,* **35,** 18–24.

——, and J. J. Finnigan, 1994: *Atmospheric Boundary Layer Flows: Their Structure and Measurement.* Oxford University Press, 289 pp.

——, J. C. Wyngaard, Y. Izumi, and O. R. Coté, 1972: Spectral characteristics of surface-layer turbulence. *Quart. J. Roy. Meteor. Soc.,* **98,** 563–589.

Katul, G. G., and M. B. Parlange, 1995: The spatial structure of turbulence at production wavenumbers using orthonormal wavelets. *Bound.-Layer Meteor.,* **75,** 81–108.

——, and C. R. Chu, 1998: A theoretical and experimental investigation of the energy-containing scales in the dynamic sublayer of boundary-layer flows. *Bound.-Layer Meteor.,* **86,** 279–312.

——, ——, M. B. Parlange, J. D. Albertson, and T. A. Ortenburger, 1995: The low wave number spectral characteristics of turbulent velocity and temperature in the unstable atmospheric surface layer. *J. Geophys. Res.,* **100,** 14 243–14 255.

——, J. D. Albertson, C. I. Hsieh, P. S. Conklin, J. T. Sigmon, M. B. Parlange, and K. R. Knoerr, 1996: The inactive eddy motion and the large-scale turbulent pressure fluctuations in the dynamic sublayer. *J. Atmos. Sci.,* **53,** 2512–2524.

Klebanoff, P. S., 1954: Characteristics of turbulence in a boundary layer with zero pressure gradient. National Advisory Committee for Aeronautics, National Bureau of Standards, Tech. Rep. 1247, 128 pp.

Kolmogorov, A. N., 1941: The local structure of turbulence in incompressible viscous fluid for very large Reynolds numbers. *Dokl. Akad. Nauk SSSR,* **30,** 299–304.

Korotkov, B. N., 1976: Some types of local self similarity of the velocity field of wall turbulent flows. *Izv. Akad. Nauk SSSR Ser. Mekh. Zhidk. I. Gaza,* **6,** 35–42.

Krettenauer, K., and U. Schumann, 1992: Numerical simulation of turbulent convection over wavy terrain. *J. Fluid Mech.,* **237,** 261–299.

Lafore, J. P., and Coauthors, 1998: The Méso-Nh atmospheric simulation system. Part I: Adiabatic formulation and control simulation. *Ann. Geophys.,* **16,** 90–109.

Lauren, M. K., M. Menabde, A. W. Seed, and G. L. Austin, 1999: Characterisation and simulation of the multiscaling properties of the energy-containing scales of horizontal surface-layer winds. *Bound.-Layer Meteor.,* **90,** 21–46.

Lin, C. L., 2000: Local pressure-transport structure in a convective atmospheric boundary layer. *Phys. Fluids,* **12,** 1112–1128.

——, J. C. McWilliams, C. H. Moeng, and P. P. Sullivan, 1996: Coherent structures in a neutrally-stratified planetary boundary layer. *Phys. Fluids,* **8,** 2626–2639.

——, C. H. Moeng, P. P. Sullivan, and J. C. McWilliams, 1997: The effect of surface roughness on flow structures in a neutrally-stratified planetary boundary layer. *Phys. Fluids,* **9,** 3235–3249.

Mayor, S. D., G. J. Tripoli, and E. W. Eloranta, 2003: Evaluating

large-eddy simulations using volume imaging lidar data. *Mon. Wea. Rev.,* **131,** 1428–1452.

Moeng, C. H., and P. P. Sullivan, 1994: A comparison of shear- and buoyancy-driven planetary boundary layer flows. *J. Atmos. Sci.,* **51,** 999–1022.

Mulhearn, P. J., and J. J. Finnigan, 1978: Turbulent flow over a very rough, random surface. *Bound.-Layer Meteor.,* **15,** 109–132.

Nicholls, S., and C. J. Readings, 1979: Aircraft observations of the structure of the lower boundary layer over the sea. *Quart. J. Roy. Meteor. Soc.,* **105,** 785–802.

Nieuwstadt, F. T. M., P. J. Mason, C. H. Moeng, and U. Schumann, 1992: Large-eddy simulation of the convective boundary layer: A comparison of four computer codes. *Turb. Shear Flows,* **8,** 343–367.

Panchev, S., 1971: *Random Functions and Turbulence.* Pergamon Press, 443 pp.

Panofsky, H. A., 1974: The atmospheric boundary layer below 150 meters. *Annu. Rev. Fluid Mech.,* **6,** 147–177.

Perry, A. E., and C. J. Abell, 1975: Scaling laws for pipe flow turbulence. *J. Fluid Mech.,* **67,** 257–271.

——, and ——, 1977: Asymptotic similarity of turbulence structures in smooth and rough walled pipes. *J. Fluid Mech.,* **79,** 785–799.

——, and J. D. Li, 1990: Experimental support for the attached eddy hypothesis in zero pressure gradient turbulent boundary layers. *J. Fluid Mech.,* **218,** 405–438.

——, S. M. Henbest, and M. S. Chong, 1986: A theoretical and experimental study of wall turbulence. *J. Fluid Mech.,* **165,** 163–199.

——, K. L. Lim, and S. M. Henbest, 1987: An experimental study of the turbulence structure in smooth and rough wall boundary layers. *J. Fluid Mech.,* **177,** 437–466.

Pond, S., S. D. Smith, P. F. Hamblin, and R. W. Burling, 1966: Spectra of velocity and temperature fluctuations in the atmospheric boundary layer over the sea. *J. Atmos. Sci.,* **23,** 376–386.

Poulos, G. S., and Coauthors, 2002: CASES-99: A comprehensive investigation of the stable nocturnal boundary layer. *Bull. Amer. Meteor. Soc.,* **83,** 555–581.

Raupach, M. R., K. A. Antonia, and S. Rajagopalan, 1991: Rough wall turbulent boundary layers. *Appl. Mech. Rev.,* **44,** 1–25.

Redelsperger, J. L., and G. Sommeria, 1981: Méthode de représentation de la turbulence d'échelle inférieure à la maille pour un modèle tridimensionnel de convection nuageuse. *Bound.-Layer Meteor.,* **21,** 509–530.

——, F. Mahé, and P. Carlotti, 2001: A simple and general subgrid model suitable both for surface layer and free-stream turbulence. *Bound.-Layer Meteor.,* **101,** 375–408.

Richards, P. J., S. Fong, and R. P. Hoxey, 1997: Anisotropic turbulence in the atmospheric surface layer. *J. Wind Eng. Ind. Aerodyn.,* **69–71,** 903–913.

——, R. P. Hoxey, and J. L. Short, 1999: Spectral models of the atmospheric surface layer. *Proc. 10th Int. Conf. on Wind Engineering,* Copenhagen, Denmark.

Schmidt, H., and U. Schumann, 1989: Coherent structure of the convective boundary layer derived from large-eddy simulation. *J. Fluid Mech.,* **200,** 511–562.

Shaw, W. J., and J. A. Businger, 1985: Intermittency and the organization of turbulence in the near-neutral marine atmospheric boundary layer. *J. Atmos. Sci.,* **42,** 2563–2584.

Smagorinsky, J., 1963: General circulation experiments with the primitive equations: I. The basic experiment. *Mon. Wea. Rev.,* **91,** 99–164.

Stevens, B., and D. H. Lenschow, 2001: Observations, experiments, and large-eddy simulation. *Bull. Amer. Meteor. Soc.,* **82,** 283–294.

Stull, R. B., 1988: *An Introduction to Boundary Layer Meteorology.* Kluwer Academic Publishers, 666 pp.

Tchen, C. M., 1953: On the spectrum of energy in turbulent shear flow. *J. Res. Natl. Bur. Stand.,* **50,** 51–62.

——, 1954: Transport processes as foundations of the Heisenberg and Obukhoff theories of turbulence. *Phys. Rev.,* **93,** 4–14.

Townsend, A. A., 1976: *The Structure of Turbulent Shear Flows.* 2d ed. Cambridge University Press, 429 pp.

Turan, Ö., R. S. Azad, and S. Z. Kassab, 1987: Experimental and theoretical evaluation of the k^{-1} spectral law. *Phys. Fluids,* **30,** 3463–3474.

Weinbrecht, S., S. Raasch, A. Ziemann, K. Arnold, and A. Raabe, 2004: Comparison of large-eddy simulation data with spatially averaged measurements obtained by acoustic tomography—Presuppositions and first results. *Bound.-Layer Meteor.,* **111,** 441–465.

Wilczak, J. M., and J. E. Tillman, 1980: The three-dimensional structure of convection in the atmospheric surface layer. *J. Atmos. Sci.,* **37,** 2424–2443.

Wulfmeyer, V., 1999: Investigations of humidity skewness and variance profiles in the convective boundary layer and comparison of the latter with large-eddy simulations results. *J. Atmos. Sci.,* **56,** 1077–1087.

Wyngaard, J. C., and O. R. Coté, 1974: The evolution of a convective planetary boundary layer: A higher-order closure model study. *Bound.-Layer Meteor.,* **7,** 289–308.

——, and L. J. Peltier, 1996: Experimental micrometeorology in an era of turbulence simulation. *Bound.-Layer Meteor.,* **78,** 71–86.

Yaglom, A. M., 1991: Similarity laws for wall turbulence flows. *New Approaches and Concepts in Turbulence,* T. Dracos and A. Tsinober, Eds., Birkhäuser, 7–27

——, 1994: Fluctuation spectra and variances in convective turbulent boundary layers: A reevaluation of old models. *Phys. Fluids,* **6,** 962–972.